# How steady are steady-state mountain belts? – a re-examination of the Olympic Mountains (Washington State, USA)

Lorenz Michel[1], Christoph Glotzbach[1], Sarah Falkowski[1], Byron A. Adams[1,2], Todd A. Ehlers[1]

[1]Department of Geosciences, University of Tübingen, Tübingen, 72074, Germany
5    [2]School of Earth Sciences, University of Bristol, Bristol, BS8 1RJ, United Kingdom

*Correspondence to*: Todd A. Ehlers (todd.ehlers@uni-tuebingen.de)

**Abstract.** The Olympic Mountains of Washington State (USA) represent the aerially exposed accretionary wedge of the Cascadia subduction zone and are thought to be in flux steady-state, whereby the mass outflux (denudation) and influx (tectonic accretion) into the mountain range are balanced. We use a multi-method approach to investigate how temporal variations in
10    the influx and outflux could affect previous interpretations of flux steady-state. This includes published and new thermochronometric ages for (U-Th)/He dating of apatite and zircon (AHe and ZHe, respectively) and fission track dating of apatite and zircon (AFT and ZFT, respectively), 1D thermo-kinematic modelling of thermochronometric data and independent estimates of outflux and influx.

We present 61 new thermochronometric ages. AHe ages are generally young (<4 Ma), and in some samples, AFT
15    ages (5–8 Ma) overlap with ZHe ages (7–9 Ma) within uncertainties. Thermo-kinematic modelling shows that exhumation rates are temporally variable, with rates decreasing from >2 km/Myr to <0.3 km/Myr around 6–8 Ma. With the onset of Plio-Pleistocene glaciation, exhumation rates increased again to values >1 km/Myr. This demonstrates that the material outflux is varying through time, requiring a commensurate variation in influx to maintain flux steady-state. Evaluation of the offshore and onshore sediment record shows, that the material influx is also variable through time and that the amount of sediment
20    residing in the wedge is spatially variable. Our quantitative assessment of influx and outflux indicates that the Olympic Mountains could be in flux steady-state on long timescales ($10^7$ yr), but significant perturbations of steady-state occur on shorter timescales ($10^5$–$10^6$ yr), e.g., during the Plio-Pleistocene glaciation.

## 1 Introduction

The assumption of a balance between opposing processes has allowed geoscientists to use proxy measurements (like
25    denudation rates) to constrain difficult to measure variables like rock uplift. This has given rise to the concept of steady-state landscapes or mountain ranges. Likewise, steady-state (i.e., a mass balance) is commonly one of the boundary conditions in modelling studies investigating the evolution and dynamics of orogens in response to changes of other boundary conditions like climate or tectonic fluctuations (e.g Batt et al., 2001; Stolar et al., 2007; Whipple and Meade, 2006; Willett, 1999). Two main types of steady-state are often used to interpret mountain building processes (e.g. Willett and Brandon, 2002): (1)

30     Topographic steady-state, where the topography is invariant, because rock uplift and horizontal motion of material is balanced by denudation, and (2) flux steady-state, where the material influx (by accretion of sediment and rock) is balanced by the material outflux (by denudation) from a mountain range. The assumption of steadiness is timescale-dependent, so that long-lived ($10^7$ yr) steady-state landscapes are unlikely, given the dynamic nature of many mountain belts. But assuming a quasi-steadiness on shorter timescales ($10^4$–$10^6$ yr), at which geomorphic processes act and common analytical techniques integrate

35     (e.g., cosmogenic nuclides, thermochronometry), seems to be plausible.

However, studies from different orogens worldwide suggest strong variations in denudation and exhumation on million-year timescales. These variations can be linked to changes in the tectonic parameters (e.g. Adams et al., 2015; Lease et al., 2016), or to changes in the climate like the magnitude of precipitation (e.g. Lease and Ehlers, 2013; Whipple, 2009) or the onset of Plio-Pleistocene glaciation (e.g. Berger et al., 2008; Ehlers et al., 2006; Glotzbach et al., 2013; Gulick et al., 2015;

40     Herman et al., 2013; Herman and Brandon, 2015; Lease et al., 2016; Thomson et al., 2010; Valla et al., 2011).

Based on thermo-kinematic modelling of thermochronometric cooling ages, the Olympic Mountains, USA, (Fig. 1a) have been interpreted to be in flux steady-state since ca. 14 Ma (Batt et al., 2001; Brandon et al., 1998). However, the impact of Plio-Pleistocene glaciation on the flux steady-state hypothesis has not been considered yet, although the range was extensively incised by glaciers (Adams and Ehlers, 2017; Montgomery, 2002; Montgomery and Greenberg, 2000; Porter,

45     1964) and experienced significant changes in climate conditions over the past 3 Myr (Mutz et al., 2018). Numerical modelling studies investigated the mechanics of the wedge by either considering fluvial erosion (Stolar et al., 2007) or glacial erosion (Tomkin and Roe, 2007). A significant response of the orogenic wedge to glaciation was suggested (Tomkin and Roe, 2007) and recent studies proposed that exhumation rates in the Olympic Mountains increased due to Plio-Pleistocene glacial erosion (Herman et al., 2013; Michel et al., 2018). Resulting high sedimentation rates seem to have caused a change in the

50     deformational style of the offshore part of the wedge (Adam et al., 2004).

In this study, we test the hypothesis of flux steady-state in the Olympic Mountains, considering variations in both the material influx and outflux. First, we test the temporal steadiness of exhumation rates from bedrock cooling histories with a 1D thermo-kinematic model incorporating multiple thermochronometers (apatite and zircon (U-Th)/He and fission-track data; AHe, ZHe, AFT, and ZFT, respectively). Second, we attempt to independently estimate both the accretionary influx and

55     denudational outflux, using published data of the off- and onshore sediment records, and exhumation rates from thermochronometry. We observe temporal variations in exhumation rates, which are interpreted to reflect changes in the tectonics (a reduction in plate subduction velocity results in a decrease in exhumation rate) and climate (Plio-Pleistocene glaciation results in an increase in exhumation rate). Likewise, both material influx and outflux are temporally variable, especially during the Quaternary. A quantitative comparison between both fluxes suggests, that the Olympic Mountains could

60     be in flux steady-state over long timescales (i.e., 14 Myr), and also demonstrates, that it is essential to consider the spatial geometry used for flux steady-state assessment (i.e., two- vs. three-dimensional).

## 2 Background

### 2.1 Geology and glacial history of the Olympic Mountains

At present, the Juan de Fuca Plate subducts obliquely with respect to the overriding North American Plate (Fig. 1a)
with 34 mm/yr at the latitude of the Olympic Mountains (Doubrovine and Tarduno, 2008). The forearc high of the subduction
zone comprises (from north to south) Vancouver Island, the Olympic Mountains and the Oregon Coast Range, and lies west
of a forearc low (e.g., Georgia Lowlands, Puget Lowlands) and the active volcanic arc (Fig. 1a). Seismic imaging suggests a
3D curvature of the down-going slab beneath southern Vancouver Island and the Olympic Mountains (Hayes et al., 2012;
McCrory et al., 2012), indicated by a flatter subduction angle under the orogen, compared to areas in the north and south of
that (Fig. 1a). The modern configuration of the subduction zone has been established by the latest Eocene (e.g., Brandon and
Vance, 1992) after accretion of the Coast Range Terrane to the North American continent. This terrane represents a large
oceanic plateau and extends from the southern tip of Vancouver Island to Oregon (Eddy et al., 2017; Phillips et al., 2017;
Wells et al., 2014).

The accretionary wedge of the subduction zone is exposed onshore within the Olympic Mountains (Fig. 1a) and is
composed of Eocene–Miocene flysch (Brandon et al., 1998; Tabor and Cady, 1978). This part of the mountain range is known
as the Olympic Structural Complex (Brandon et al., 1998) and is separated from the surrounding Coast Range Terrane by the
Hurricane Ridge thrust fault (HRF in Fig. 1c), a major discontinuity traceable in seismic surveys (e.g., Clowes et al., 1987;
Calvert et al., 2011). Minor sedimentary rocks of Eocene age (Eddy et al., 2017; Tabor and Cady, 1978) are contained within
the Coast Range Terrane besides the predominant ~50 Ma old marine and subaerial basaltic rocks (Eddy et al., 2017).
Exhumation of the range commenced at 18 Ma and since 14 Ma, the orogen is supposed to be in flux steady-state (Batt et al.,
2001; Brandon et al., 1998).

Plio-Pleistocene glaciation has strongly influenced the present-day appearance of the Olympic Mountains (Fig. 1b).
During its maximum extent at ~14 ka, the Cordilleran Ice Sheet advanced from the Coast Mountains of British Columbia and
covered Vancouver Island and large parts of todays' continental shelf (Booth et al., 2003; Clague and James, 2002). The Puget
and Juan de Fuca lobe of the Cordilleran Ice Sheet surrounded the Olympic Mountains in the east/southeast and in the north,
respectively (Fig. 1b). Alpine glaciers incised deep valleys in the landscape, particularly on the western side of the range
(Adams and Ehlers, 2017; Montgomery, 2002), where piedmont glaciers almost reached the Pacific Ocean (Thackray, 2001).
Glacial erosion varied across the range, as the location of the Pleistocene equilibrium line altitude increases from 1000 m in
the west to 1800 m in the east (Porter, 1964), due to a strong precipitation gradient (> 6000 mm/yr in the west, < 1000 mm/yr
in the east). Determining the exact onset of glaciation in the Olympics has proven difficult, but the oldest deposits of the
Cordilleran Ice Sheet in the Puget Lowland are as old as 2 Ma and deeply weathered alpine till on the west side of the Olympics
is interpreted to be of the same age (Easterbrook, 1986).

## 2.2 Previous thermochronometry studies in the Olympic Mountains

Within the Olympic Mountains, an extensive dataset of thermochronometric cooling ages from bedrock samples (Fig.
95    1b, 2) exists for AHe (Batt et al., 2001; Michel et al., 2018), AFT (Brandon et al., 1998), ZHe (Michel et al., 2018) and ZFT
(Brandon and Vance, 1992; Stewart and Brandon, 2004). These thermochronometer systems have effective closure
temperatures of 60–70°C, 100–120°C, ~180°C and ~240°C for a cooling rate of ~10 °C/Myr, respectively (Ehlers, 2005). The
interpretation of thermochronometric cooling ages from sedimentary rocks (such as in the Olympic Mountains) is often
complicated, when the cooling signal from the sediments' source region(s) has not been reset due to reheating during
100    subduction and metamorphism. If a sedimentary rock sample has not had sufficient exposure to temperatures above the closure
temperature of a given thermochronometer, the sample might retain cooling ages that represent the source region's cooling
history (unreset sample) or might be a mixture of these cooling histories and the reheating process (incompletely reset sample).
Determining, whether a sample is completely, incompletely or un-reset can be difficult and usually depends on the statistics
of cooling age populations, derived from the dated mineral grains (e.g. Brandon et al., 1998). The reproducibility of single
105    grain (U-Th)/He ages from a sample provides an indication of whether a sample is reset or not. This is typically determined
with n=4–7 grains. For the fission track method a large number of grains is typically dated (n=20–100) for cost and analytical
reasons. Statistical methods can be applied (Brandon, 1992, 1996), allowing to decompose the grain age distribution into grain
age populations and to determine, if the sample is reset, incompletely reset or unreset. In case a sample is incompletely reset,
the peak age of the youngest age population is usually interpreted as the sample age (e.g., Brandon et al., 1998).

110    In the Olympics, the youngest reset AHe ages (≤ 2.5 Ma) can be found in the western and central part of the mountain
range and there are also two unreset samples in the eastern part (Fig. 2a). The pattern of AFT ages is more complicated (Fig.
2b) and most fully reset and incompletely reset samples are located in the central part of the mountain range, whereas unreset
samples are restricted to areas outside the central (high topography) part of the range. The youngest reported AFT samples (2–
4 Ma) are incompletely reset samples and fully reset samples have cooling ages between 7 Ma and 27 Ma. ZHe data show a
115    well-developed trend of unreset cooling ages at the coast and reset 5–6 Ma ages in the headwaters of Hoh and Elwha rivers
(cf., Fig. 1b, Fig. 2c). Reset ZFT samples (~13–14 Ma) are confined to a small area east of Mt. Olympus (Fig. 2d).

Based on thermo-kinematic modelling, Michel et al. (2018) attributed the observed AHe and ZHe age pattern to an
ellipse-shaped exhumation pattern (with highest exhumation rates in the central, high-topography part of the mountain range,
Fig. 2e), as predicted for a mountain range situated in an orogenic syntaxis setting (Bendick and Ehlers, 2014). Here, a bend
120    in the subducted slab creates a mechanical stiffening, which in turn leads to rapid and focused exhumation at the surface
(Bendick and Ehlers, 2014). High uplift rates in the central, high topography part of the mountain range are also corroborated
by topographic analyses (Adams and Ehlers, 2017) and denudation rates based on cosmogenic nuclides (Adams and Ehlers,
2018). Furthermore, modelling of particularly young AHe ages (<2.5 Ma) suggests, that exhumation rates increased
significantly by 50–150 % due to Plio-Pleistocene glacial erosion (Michel et al., 2018).

### 2.3 Offshore sediment record

Three boreholes were drilled into the blanketing sediments during deep-sea drilling projects (ODP 888, ODP 1027 and DSDP 174; Fig. 3 and Table 1) and results from three seismic studies (Adam et al., 2004; Booth-Rea et al., 2008; Han et al., 2016) give information close to the deformation front (Fig. 3). These data provide constraints on the sediment thickness and sedimentation rates before incorporation of sediment into the accretionary wedge.

Most of the sediment is contained within two deep-sea sediment fans with different sediment sources. Today, sediment sources for the Nitinat Fan (offshore Vancouver Island and the Olympic Mountains) include detritus from Vancouver Island, the Olympic Mountains, and material delivered by the Fraser river system (Fig. 3), which drains large parts of the Canadian Cordillera including the British Columbian Coast Mountains (Carpentier et al., 2014; Kiyokawa and Yokoyama, 2009). The Astoria Fan offshore the Oregon coast is mostly fed by the Columbia River and is sourced by a large area in the interior of the USA (Fig. 3).

The total sediment thickness varies between 2600–3500 m at the deformation front and decreases rapidly to 600 or 900 m approximately 100 km away from the deformation front. At ODP 1027 and DSDP 174, up to 50–70 % of the total sediment thickness are Quaternary deposits, and sedimentation rates more than doubled during the Quaternary (from 80–110 m/Myr to 250–270 m/Myr, Table 1). At ODP 888 the drilled 570 m of core were deposited over the past 600 kyr, suggesting very high sedimentation rates of 950 m/Myr compared to 400 m/Myr for the total sediment thickness of 2600 m at the location of the core (Table 1). As determined from detailed, stratigraphic analysis of core ODP 888, sedimentation rates are also highly variable during the Quaternary itself; rates during glacial periods can be as high as 1900 m/Myr compared to 700 m/Myr during interglacials (Knudson and Hendy, 2009). At sites ODP 888 and 1027, the source region of the sediments has been the Canadian Cordillera for the past 3.5 Myr, which has not been affected by glacial-interglacial cycles (Carpentier et al., 2014; Kiyokawa and Yokoyama, 2009). The provenance of the sediments at DSDP 174 is mostly the Proterozoic Belt Supergroup in the interior of the USA and differs significantly from present-day detritus of the Columbia River (Prytulak et al., 2006). Hence, Prytulak et al. (2006) suggest that deposition of the upper 630 m of sediment at this site and the build-up of the Astoria Fan were governed by glacial outburst floods.

### 3 Methods

We use a multi-method approach to assess flux steady-state in the Olympic Mountains. This includes thermochronometric dating, thermo-kinematic modelling of cooling ages to obtain exhumation rates, and independent estimates of accretionary influx and denudational outflux from the sedimentary record. The procedure for each method is outlined below.

## 3.1 Thermochronometric methods

155    We present 19 new bedrock samples from vertical profiles (Fig. 4, Table 2) and two additional bedrock samples (OP1528 and OP1556; Fig. 4a, Table 2) collected at an elevation of ~400 m, enlarging the existing ~400 m equal-elevation data of Michel et al. (2018). All new samples are sandstones of varying grain size. A sample transect at Mt. Olympus extends from the bottom of the Hoh Valley to the apex of the Olympic Peninsula (Mt. Olympus, 2428 m), covering ~2 km of relief (Fig. 4a,b). The Mt. Anderson transects starts in the upper reaches of the Quinault Valley and terminates on the flank of Mt.

160    Anderson covering a total elevation difference of ~1600 m (Fig. 4a,c). The Blue Mountain transect is located in the northern part of the Olympic Peninsula close to Blue Mountain, covering an elevation difference of ~1300 m (Fig. 4a,d).

All collected samples were dated with the AHe and ZHe techniques, whereas three/two were also dated by AFT/ZFT technique. Additionally, we dated 13 samples from Michel et al. (2018) by AFT and five of these by ZFT thermochronometry. In summary, for seven samples AHe, AFT, ZHe and ZFT cooling ages are available (Table 2). Standard mineral separation

165    techniques (sieving, magnetic and gravimetric separation) were used to obtain apatite and zircon separates from crushed rock samples.

Mineral grains were hand-picked and dated in the thermochronometry lab of the University of Tübingen for AHe and ZHe dating, following the dating protocol of Stübner et al. (2016). The Ft-correction for apatite (Farley, 2002) and zircon (Hourigan et al., 2005) is applied to the measured amount of helium. The (U-Th)/He age equation is solved using the approach

170    of Meesters and Dunai (2005). From each sample, we date 4–7 apatite grains or 3–6 zircon grains and the results for the single-grain analyses can be found in Tables S1 and S2, respectively. Our approach for assessing whether a sample is reset or unreset and the procedure for exclusion of outliers is explained in the supplementary material. For reset samples, we calculate the arithmetic mean age from the accepted single grain ages, which is reported in Table 2 as sample age together with one standard deviation (1SD) as uncertainty.

175    Fission-track dating of apatite and zircon is performed using the external detector and the ζ-calibration techniques (Hurford, 1990). Details about the treatment of the apatite and zircon mounts in the Tübingen themrochronometry laboratory can be found in Falkowski et al. (2014) and Falkowski and Enkelmann (2016). Table 3 contains the AFT and ZFT sample ages, and explains the procedure for assessing, whether a sample is reset or unreset, together with the procedure used for decomposing the grain age distribution (in case a sample is unreset). Data for single grain ages from fission-track dating of

180    apatite and zircon are reported in Tables S3 and S4.

## 3.2 Thermo-kinematic modelling: model setup and boundary conditions

To connect cooling histories recorded by our thermochronometers to exhumation histories, we used a modified version of the thermo-kinematic model Pecube (Braun, 2003), which contains a built-in Monte Carlo approach to resolve temporal variations in exhumation histories (Adams et al., 2015; Thiede and Ehlers, 2013). The model allows exploring

185    possible exhumation histories by varying exhumation rates through time at defined time steps. The probability of a particular

exhumation rate history is estimated by comparing modelled with observed cooling ages. In order to generate well-constrained models, we use the seven samples for which we have AHe, AFT, ZHe, and ZFT ages (OP1513, OP1517, OP1533, OP1539, OP1551, OP1573, OP1582; Table 2).

190  Thermo-physical parameters chosen for the modelling are typical values reported for the sandstones of the Olympic Mountains (Table 4). We initiate the models at 20 Ma and use a time-step interval of 1 Myr with a maximum exhumation rate of 6 km/Myr. For each sample, we run 20,000 simulations (each corresponding to a different exhumation history) and assess the goodness of fit between observed and modelled data for the respective exhumation history, using a reduced $\chi^2$-test. Here, sample ages $\tau_o$ are compared with modelled ages $\tau_m$, using the uncertainty of the sample age $\sigma_o$ for the number (N) of thermochronometer systems available for the respective sample:

195
$$\chi^2 = \left( \left( \frac{(\tau_o - \tau_m)^2}{\sigma_o} \right)_{AHe} + \left( \frac{(\tau_o - \tau_m)^2}{\sigma_o} \right)_{AFT} + \left( \frac{(\tau_o - \tau_m)^2}{\sigma_o} \right)_{ZHe} + \left( \frac{(\tau_o - \tau_m)^2}{\sigma_o} \right)_{ZFT} \right) \cdot \frac{1}{N} \quad (1)$$

If $\chi^2 \leq 2$, a specific model run is accepted as good. The number of accepted model runs (exhumation histories) is shown in Fig. 5 for each sample. From the range of acceptable exhumation rates at each time step (shown as bluish shaded areas in Fig. 5), we calculate the mean exhumation rate together with 1 standard deviation for each time step (red/dashed lines and grey areas in Fig. 5). Although the model provides output for the entire model duration (i.e., 20 Myr), a meaningful exhumation

200  rate can only be obtained for the time interval between oldest thermochronometric age of a sample and today (shown in Fig. 5).

For our purpose, we want to focus on exploring temporal variations in exhumation rates and therefore use a 1D model, where each sample is modelled independently from each other. Here, heat transport and movement of particles is only considered in one dimension within a column of rock, ignoring topography. This is a simplification compared to previous,

205  more sophisticated models in the study area (e.g. Batt et al., 2001; Michel et al., 2018). On the other hand, it allows to perform thousands of simulations and to cover a large range of possible exhumation rates, in order to have a robust statistical assessment of the best-fitting exhumation history. Previous publications in other orogens have also highlighted, that 1D models only considering vertical transport of heat are often sufficient to explain most of the signal recorded in thermochronometric systems (e.g., Adams et al., 2015; Thiede and Ehlers, 2013). In the Olympic Mountains, Michel et al. (2018) also argued, that

210  exhumation histories for the thermochronometer systems considered here can be well explained by vertical velocity paths. A limitation in a 1D modelling approach is its inability to resolve topographic controls on near surface isotherms, or resolve paleotopographic changes. So we limit our interpretations of the resolved exhumation histories to focus on the primary temporal changes, rather than paleotopography, or specific differences in the exhumation rates between samples.

Five of the seven considered samples are from the same elevation range (400–580 m), but two samples are from higher

215  elevations (1360 m and 1500 m, Fig. 5). Large differences in elevation between the samples can impact the direct comparison between them (e.g., it can shift the time when a change in exhumation rate occurred). However, we are not able to correct for this circumstance (e.g., by using an age elevation relationship), but try to consider this complication, when interpreting our exhumation rate histories from the different samples.

### 3.3 Methods for estimating flux steady-state

220    To assess the flux steady-state hypothesis of the Olympic Mountains, we need independent estimates of the material influx and outflux over time. For this, we focus on the time period since 14 Ma, which corresponds to the proposed establishment of flux steady-state (Batt et al., 2001; Brandon et al., 1998).

Flux steady-state requires that the material influx into the wedge equates the amount of accreted material, scraped off from the subducting slab at the deformation front (Fig. 6a). We assessed the amount of accreted sediment (material influx)

225    with two approaches. First, we calculated the amount of sediment incorporated into the accretionary wedge at the deformation front during the 14 Myr period. Second, we compared this amount of "expected" accreted sediment with the observed amount of sediment residing in the accretionary wedge along two cross sections. We estimated the material outflux from the mountain range using results from thermo-kinematic modelling, by equating modelled exhumation with denudation, which can then be integrated spatially and over the 14 Myr period.

230    To make the calculations of both fluxes directly comparable, it is essential to consider the spatial geometries, used for calculating the fluxes. E.g., if exhumation rates are integrated along a profile spanning the Olympic Peninsula (so a two-dimensional geometry, dashed line in Fig. 6c), then the material influx occurs within a vertical column at a single location at the deformation front (Fig. 6a). If exhumation rates are integrated over an area (so a three-dimensional geometry, entire exhumation pattern in Fig. 6c), then the material influx into this area has to be considered. Hence, the influx occurs within a

235    vertical plane and needs to be calculated over a distance along the deformation front (Fig. 6a). We provide estimates for both the influx and outflux using a two-dimensional and three-dimensional geometry, respectively.

### 3.3.1 Calculating the accretionary influx

We applied a similar approach as Batt et al. (2001) to calculate the accretionary influx, but we also considered temporal variations of the used variables. Assuming all sediments resting on the subducting oceanic crust are incorporated into the

240    accretionary wedge, the volume of accreted sediment ($V_{sed}$) can be approximated using the porosity of the sediment $\eta$, incoming sediment thickness d, the duration of subduction t, and the subduction velocity perpendicular to the present-day deformation front $u_{per}$:

$$V_{sed} = \eta \cdot d \cdot t \cdot u_{per} \quad (2)$$

A limitation to this approach might be, if not all sediment resting on the down going plate is accreted. There is

245    geochemical evidence, that at early stages of subduction at the Cascadia Subduction zone, sediment has been incorporated into the mantle and been involved in the magmatism of the Cascades Arc (Leeman et al., 2005; Mullen et al., 2017). However, there are no estimates on the amount of sediment transported to the mantle at present, and most sediments seem to be accreted, either at the deformation front or underplated at depth (Calvert et al., 2011).

The variable with the greatest uncertainty in this calculation is the sediment thickness. As discussed above (Sect. 2.3),

250    the present-day sediment thickness is the product of increased offshore sedimentation during the Quaternary, and the pre-

Quaternary sediment thickness is difficult to estimate. Therefore, we calculated three different sediment volumes based on different sediment thicknesses (Table 5). Assuming a thickness of 1.5 km and 2.5 km for the 14 Myr period yields a minimum and maximum value, respectively, representing a sediment volume unaffected by Quaternary sedimentation (1.5 km) and a volume for a likely too high sediment thickness, using today's thickness (2.5 km). Alternatively, we considered an increase in

255    sediment thickness from 1.5 km to 2.5 km at 2 Ma, which likely yields the geologically most meaningful volume.

The porosity of the sediment stack depends on the thickness and decreases with increasing overburden. According to (Yuan et al., 1994), the porosity at depth z of the sediment stack can be approximated by

$$\eta = 0.6 \cdot e^{-z} \quad (3)$$

Using this equation, we calculated mean porosities of 31% and 22% for our sediment thicknesses of 1.5 km and 2.5 km,

260    respectively.

Because the dip direction of the present-day deformation front is 72° ($\Phi_{def}$) and we only considered accretion perpendicular to the deformation front, we corrected the convergence rate (u) by using the convergence angle ($\Phi$) between the Juan de Fuca and the North American plates:

$$u_{per} = u \cdot \frac{\sin(\phi)}{\sin(\phi_{def})} \quad (4)$$

265    Both convergence rate and angle are variable over time and, therefore, we capitalized on the plate reconstruction model of (Doubrovine and Tarduno, 2008) to estimate these parameters over the past 14 Myr. Values shown in Fig. 6b and 6c were calculated using the East-West Antarctica plate circuit model of (Doubrovine and Tarduno, 2008) for two different rotation models (Farallon M1 and M2 in the original publication). This yields a range of possible convergence rates and angles, providing an uncertainty on the calculated sediment volume. The temporal resolution is given by the number of magnetic

270    isochrons used for the plate circuit reconstruction in (Doubrovine and Tarduno, 2008).

From the temporal evolution of the corrected convergence rate (Fig. 6b), we calculated the sedimentary volume $V_{sed}$ accreted during the 14 Myr period using Eq. 2 and the parameters mentioned above. We report sediment volumes for two-dimensional and three-dimensional accretionary influx (Table 5). For the two-dimensional scenario, sediment can be viewed as being accreted at a single vertical column at the deformation front (Fig. 6a). For the three-dimensional scenario, accretion

275    occurs along a vertical plane at the deformation front (Fig. 6a), and results obtained from Eq. 2 are multiplied by a length (l). Both the coastline and the deformation front are approximately parallel at the latitude of the Olympic Mountains. Hence, the length of the coastline in the area used for integrating the exhumation rates corresponds to the required length of the deformation front. This yields a value of 131 km for the length (l) used in our calculations (see Fig. 6d).

### 3.3.2 Sediment volumes along cross sections

280    We estimated the actual volume of sediment currently residing in the accretionary wedge along two cross sections, extending from the deformation front across the Olympic Peninsula, approximately 50 km apart (Profile 1 and 2 in Fig. 7). The lower boundary of the accretionary wedge is the top of the subducting oceanic plate, which is constrained from the Slab

1.0 model (Hayes et al., 2012; McCrory et al., 2012). The upper boundary is defined by the present-day topography/bathymetry (from 10 m and 500 m digital elevation models, respectively) and the Hurricane Ridge Fault (HRF). At the surface, the location

285    of the HRF is taken from a geologic map (Tabor and Cady, 1978) and below the surface we use information provided by a seismic study at depths of 22 km and 34 km (Calvert et al., 2011). The uncertainty related to the position of the HRF (error bars at HRF nodes in Fig. 7) was propagated to estimate an uncertainty for the calculated sediment volumes. Further explanation of this approach is given in the supplementary material. Because the HRF is not resolved at greater depths, we truncate the area considered for volume calculation at 34-km depth. Finally, the calculated volume is corrected for the porosity

290    of the sediment stack, assuming an average porosity of 6%, similar to Davis and Hyndman (1989).

### 3.3.3 Calculating the denudational outflux

In the absence of extensional faults, denudation acts as the prime mechanism for exhumation in the Olympic Mountains. Therefore, exhumation can be equated with denudation and the denudational outflux from the range can be obtained from the spatial and temporal integration of exhumation rates.

295    Our exhumation rates presented in this paper (Fig. 5) have a high temporal resolution, and hence provide qualitative information about variations in the denudational outflux. The sparse spatial density of the seven considered samples prohibits a quantitative assessment of the denudational outflux. To overcome this problem, we reverted to the pattern and exhumation rates suggested by Michel et al. (2018), providing good spatial coverage of almost the entire Olympic Peninsula (Fig. 6d). Furthermore, the total amount of exhumation (which is used for calculating the outflux) is similar for the two data sets. I.e., in

300    both cases the modelled exhumation rate is sufficient to explain, for instance, the ZHe age of 10.2 Ma for sample OP1513 and hence the total amount of exhumation (which corresponds to the temporal integration of the exhumation rates) is similar.

Using the pattern and rates displayed in Fig. 6d, we considered the outflux in a two- and three-dimensional scenario, to compare the obtained values with values derived from the two- or three-dimensional influx calculations. In the two-dimensional scenario, we extracted the exhumation rates along a line, crossing the Olympic Peninsula (Fig. 6d) and the values

305    for the integrals along this line are shown in Fig. 6e. In the three-dimensional scenario, we spatially integrated over the entire pattern of exhumation rates (Fig. 6d). In both scenarios, we integrated over the 14 Myr period, to derive a volume of denuded material. Because exhumation rates increased due to Plio-Pleistocene glacial erosion (Michel et al., 2018), we considered a constant exhumation scenario as well as an increase in rates (Fig. 6e). In Table 5, we report denuded volumes for the case of constant exhumation rates, for a 50% increase in rates occurring at 3 Ma, and for a 150% increase in rates occurring at 2 Ma.

310    ## 4 Results

### 4.1 Thermochronometry

Along the Mt. Olympus elevation transect (Fig. 4b), AHe ages (1.9–3.7 Ma) overlap with each other within sample error (except for the uppermost sample). ZHe ages (4.8–8.5 Ma) do likewise (with the exception of the lowermost sample; Fig.

4b). Obtained ZFT ages of this transect are all unreset. Within the Mt. Anderson transect (Fig. 4c), AHe ages (1.5–3.9 Ma)
315  increase with elevation up to an elevation of 1400 m and decrease between 1400 and 2100 m. ZHe ages (6.5–8.9 Ma) show a
similar pattern, however uncertainties for most samples are large. For the Blue Mountain transect (Fig. 4d), AHe ages (3.6–
30.1 Ma, and one unreset sample) do not show a clear correlation with elevation, but, interestingly, the uppermost sample
yields the youngest age. ZHe ages of dated samples of this transect are all unreset.

Clear spatial patterns for the multi-dated thermochronometer samples are observable (cf., Fig. 2 and 4). AHe ages are
320  reset (apart from one sample in the north-east of the mountain range) and decrease towards the centre of the mountain range,
where very young ages (< 2.5 Ma) can be found. Seven fully reset AFT samples (5.0–7.8 Ma) are confined to the centre of the
range (OP1513, OP1517, OP1533, OP1539, OP1551, OP1573, OP1582), overlapping with the area of reset ZHe samples. The
remaining eight AFT samples are unreset (Table 3 and Fig. 4). Two samples at the north and east coast (OP1502 and OP1510)
have the youngest age peaks at 26 Ma (comprising 29% of the sample's grains) and 36 Ma (35%), respectively. Samples from
325  the western part of the mountain range (OP1521, OP1522, OP1527, OP1528, OP1531) have younger age peaks of 5–16 Ma
(comprising 20–76% of the samples' grains). Furthermore, the youngest age peak of these samples decreases in age towards
the area of fully reset AFT samples.

We also collected samples (OP1527 and OP1528) next to the youngest AFT ages of Brandon et al. (1998), which were
reported as incompletely reset samples (with sample ages of 3.9 and 2.3 Ma, respectively). In the original publication, only a
330  small number of grains were dated (n=31 and n=12, respectively). To improve the statistics of these two samples, we merge
our single grain ages with those of Brandon et al. (1998) and obtain more robust age distributions (n=134 and n=80; Table 3).
The youngest peak ages of the age populations for the two merged samples are 7.4 Ma and 4.7 Ma, i.e., 2–4 Myr older than
age populations reported by Brandon et al. (1998).

ZHe ages constrain an area of reset ages (4.8–10.2 Ma) in the central, high topography part of the mountain range (light
335  grey-shaded area in Fig. 4a). Five of these samples have AFT (5.1–7.8 Ma) and ZHe (4.8–8.9 Ma) ages that overlap within
sample errors, implying rapid cooling (and hence fast exhumation) through both systems' closure isotherms. AHe ages of these
samples are much younger (1.7–3.9 Ma) and do not overlap with AFT ages, indicating that exhumation rates decreased after
cooling below the AFT closure isotherm.

Of the seven samples dated with the ZFT method, only sample OP1539 has a fully reset age (12.6 Ma). Together with
340  data from Brandon and Vance (1992) and Stewart and Brandon (2004) this confines reset ZFT samples to a very small area
east/southeast of Mt. Olympus, encompassing the headwaters of Elwha and Quinault rivers (area outlined with a red dashed
line in Fig. 4a).

## 4.2 Exhumation histories from thermo-kinematic modelling

Between 13,000–17,800 simulations provide a good fit to the data for each of the seven samples used in the thermo-
345  kinematic modelling, (Fig. 5). As expected, the four samples (OP1533, OP1539, OP1552, OP1582; Fig. 5) with overlapping
AFT and ZHe ages require fast exhumation rates of >3 km/Myr at times between 5 Ma and 8 Ma, followed by a drop in rates

to <0.2 km/Myr at 5 Ma or 7 Ma. The drop from fast to slower rates for sample OP1573 occurs at ~9 Ma. However, for this particular sample the AFT age has a larger uncertainty, hence we consider the 7–5 Ma decrease in exhumation rates as a more robust signal. Six of the seven samples (with the exception of sample OP1517) also record an increase in exhumation rates at 350 2–3 Ma to rates >1 km/Myr.

## 4.3 Estimating the flux steady-state balance

The calculated volumes of the accretionary influx depend strongly on the considered incoming sediment thickness (Table 5). In the two-dimensional scenario, volumes vary between ~530 km$^3$ (for a 1.5 km sediment thickness), ~600 km$^3$ (for an increasing sediment thickness from 1.5 km to 2.5 km at 2 Ma), and ~1000 km$^3$ (for a 2.5 km sediment thickness). In the 355 three-dimensional scenario, where accretion is considered along a length of 131 km (cf., Sect. 3.3.1), volumes vary between ~70,000 km$^3$ (1.5 km), ~76,000 km$^3$ (1.5 km to 2.5 km at 2 Ma) and ~130,000 km$^3$ (2.5 km).

The estimated amount of sediment actually residing in the accretionary wedge varies with latitude (Fig. 7). Offshore Vancouver Island, 950–1,000 km$^3$ of sediment is contained in the wedge (Davis and Hyndman, 1989), whereas on the Olympic Peninsula up to ~5,300 km$^3$ and 3,600 km$^3$ of sediment is contained within the central and southern parts of the mountain 360 range, respectively.

Our estimates of the denudational outflux vary for the different exhumation rate scenarios (Table 5). In the two-dimensional scenario (where exhumation rates are considered along a trench-perpendicular profile, Fig. 6d), the volume of denuded material is 960 km$^3$ for constant exhumation rates. Estimated volumes increase to 1060–1160 km$^3$, if an increase in exhumation rates due to Plio-Pleistocene glaciation is considered. In the three-dimensional scenario (where denudation is based 365 on the entire ellipse-shaped exhumation rate pattern, Fig. 6d), volumes are 72,000 km$^3$ for constant exhumation rates and 80,000–88,000 km$^3$ for the exhumation scenario with increasing rates.

## 5 Discussion

Above, we reported observations from different datasets or methods and the implications of each dataset will be discussed in the following. The overarching aim is to assess the flux steady-state balance between accretionary influx and 370 denudational outflux within the Olympic Mountains. Therefore, it is pivotal to have both a temporal and spatial understanding of exhumation occurring in the Olympic Mountains (because the denudational outflux is linked to exhumation). So, first we elaborate on results from thermochronometric dating, including the applicability of age elevation transects to reconstruct exhumation rates (Sect. 5.1) and the general pattern of exhumation (based on the spatial distribution of cooling ages, Sect. 5.2). Linking thermochronometric cooling ages with thermo-kinematic modelling reveals the temporal evolution of 375 exhumation rates (Sect. 5.3). Finally, we discuss the outcome of our qualitative and quantitative assessment of flux steady-state in the Olympic Mountains (Sect. 5.4).

## 5.1 Age-elevation transects

In the absence of strong, lateral gradients in exhumation rates, age-elevation transects can be used to determine an apparent exhumation rate by fitting a line through samples' cooling ages collected at a quasi-vertical elevation profile (e.g.
380  Fitzgerald et al., 1993; Reiners et al., 2003). However, the applicability of age-elevation transects to directly reconstruct exhumation rates or temporal changes in exhumation is challenging for our three transects, due to the strong spatial gradient in exhumation rates occurring in the Olympic Mountains (Michel et al, 2018; see also Fig. 2e). At Mt. Olympus (Fig. 4b) the age-elevation relationships for AHe and ZHe ages suggest fast exhumation rates. At Mt. Anderson (Fig. 4c), a break in slope at ~1400 m and decreasing ages for both AHe and ZHe at higher elevations is present in this age-elevation transect.
385  Conventionally, a change in the slope would be related to a change in exhumation rates. However, a reversal in the age-elevation relationship for AHe can also be caused by a change in relief (e.g., Braun, 2002), but it is expected to be less prominent or even absent in thermochronometers with higher closure temperature (e.g., ZHe system with a closure temperature of ~180°C). Instead we interpret the observed breaks in slope in the AHe and ZHe systems to be a result of the strong spatial variation in exhumation rates along the horizontal distance of the transect (e.g., rates increase from 0.25 km/Myr to 0.9 km/Myr
390  over a horizontal distance of 15–20 km, see Fig. 2e).

In case of the Blue Mountain transect (Fig. 4d), we relate the un-correlation of AHe ages and elevation to incomplete resetting of the AHe system in this area. Here, some samples experienced high enough temperatures to start or even complete resetting of the AHe thermochronometric system, causing the observed variability in AHe ages. Indeed, the Blue Mountain transect belongs to the Coast Range Terrane (CRT), which is at a structurally higher level compared to the actual accretionary
395  wedge (Fig. 1c).

As a summary, the observed changes in age with elevation for our age elevation transects are affected by the variation of age with elevation, the lateral variation in exhumation rates between the samples, or incomplete resetting of thermochronometer systems. Hence, no exhumation rates or temporal variations in rates can be directly determined from our transects.

400  ## 5.2 Pattern of exhumation

Different exhumation rate patterns exist for the Olympic Mountains, locating the area of fastest exhumation rates either in the central part of the mountain range (Fig. 2e) or in the western part (Fig. 2f). A well constrained spatial pattern of exhumation is needed for calculating the denudational outflux. Looking at the spatial distribution of thermochronometric cooling ages provides qualitative information about the pattern of exhumation.

405  In general, the thermochronometric age pattern indicates that in the Olympic Mountains exhumation increases from the coast to the centre. As discussed above, areas belonging to the Coast Range Terrane (close to the coast or the Blue Mountain area, where unreset AHe ages can be found, Fig. 2e) correspond to the structurally highest parts within the range (Fig. 1c) and were not sufficiently reheated to reset the AHe system. Assuming a geothermal gradient typical for the Cascadia Subduction

zone of ~20 °C/km (Booth-Rea et al., 2008; Hyndman and Wang, 1993), an AHe closure temperatures of ~60–70°C, the
410 cumulative exhumation magnitude since onset of exhumation at ~18 Ma cannot have been greater than 2–3 km.

The actual accretionary wedge (the Olympic Structural Complex, cf. Fig. 1c) records exhumation from greater depths.
Here, all samples yield reset AHe ages, requiring a minimum exhumation depth of 2–3 km. In the centre of the mountain range
(encompassing the headwaters of Hoh, Queets, Quinault and Elwha rivers cf. Fig. 1b) the area of reset AFT ages approximately
overlaps with the area of reset ZHe ages (Fig. 4a), requiring deeper exhumation, compared to the coastal part of the Olympic
415 Structural Complex.

The area east/south-east of Mt. Olympus (corresponding to the area of reset ZFT samples, Fig. 4a) has been exhumed
from the greatest depths within the Olympic Mountains. For an average ZFT closure temperature of ~240 °C (Ehlers, 2005)
and the above geothermal gradient this corresponds to a maximum exhumation from depths of 10–12 km, confirming previous
estimates (Brandon and Calderwood, 1990; Brandon and Vance, 1992).

420 Summarizing, the central, high topography part of the mountain range corresponds to the most deeply exhumed part.
This corroborates the exhumation rate pattern (Fig. 2e) suggested by Michel et al. (2018), the pattern of denudation rates based
on cosmogenic nuclide dating (Adams and Ehlers, 2018), and results from topographic analysis (Adams and Ehlers, 2017),
which all suggest that most of the exhumation/denudation occurs at this location. Hence, using a similar pattern during
calculation of the denudational outflux seems to be appropriate.

425 **5.3 Temporal variations in exhumation**

Our new thermo-kinematic modelling revealed temporal variations in exhumation rates in the Olympic Mountains
(Fig. 5). The decrease of exhumation rates at 5–7 Ma can be readily explained by the reduction in plate convergence rate and
the change in convergence direction (Fig. 8). A Pacific-wide reorganization of plate movement at 5.9 Ma has been suggested
(Wilson, 2002), and rapid uplift of the Oregon Coast Range at 6–7.5 Ma with a subsequent cessation in uplift has also been
430 attributed to variations in the plate subduction parameters (McNeill et al., 2000). Furthermore, the volcanic record of the
Cascadia Subduction zone shows temporal variations, where the strongest volcanic activity lasted from 25 Ma until 18 Ma (du
Bray and John, 2011). A period of volcanic quiescence, lasting from 17 Ma until 8 Ma, was then followed by increased activity,
starting at ~7 Ma. A change in the stress field of the Cascadia Subduction zone occurred at 7 Ma, which likely also affected
the composition of the magmatism (Priest, 1990). Therefore, we interpret our observed 7–5 Ma drop in exhumation rates in
435 the Olympic Mountains as a response to changes in the plate tectonic parameters, i.e., a reduction in plate convergence rate
and change in the convergence direction.

In contrast, the increase in exhumation rates at ~2 Ma indicates a response to climatic rather than tectonic changes.
As previously suggested by Michel et al. (2018), increased denudation due to the heavy glaciation of the mountain range led
to an increase in exhumation rates by 50–150%, starting at 2–3 Ma. Our study corroborates these findings and shows that the
440 observed young AHe ages require a recent increase in exhumation rates from slower rates (<0.2 km/Myr) lasting from 7 Ma
until ~2 Ma. Glaciation of the North American continent commenced at 2.7 Ma (Haug et al., 2005) and the oldest glacial

deposits within the Olympics could be as old as 2 Ma (Easterbrook, 1986), overlapping with our modelled increase in rates at ~2 Ma. Due to the strong spatial variation of the Pleistocene equilibrium line altitude within the Olympic Mountains (Porter, 1964), glacial erosion likely also varied spatially, which could explain the different magnitude in increase of exhumation rates suggested for the different samples. Increased offshore sedimentation related to sediment contributed by glacial erosion also affected the deformational style of the offshore wedge leading to formation of landward vergent thrust faults, which changed at ~1.5 Ma (Adam et al., 2004; Flueh et al., 1998; Gutscher et al., 2001).

Taken together all data indicate that temporal variations in exhumation rates within the Olympic Mountains are subject to both changes in the tectonic and climatic conditions. The implication of these variations should be considered for the flux steady-state assessment.

### 5.4 Flux steady-state in the Olympic Mountains

### 5.4.1 A qualitative perspective

Several variables that affect both the accretionary influx and the denudational outflux show temporal variations. Exhumation rates decrease at ~6 Ma and increase at ~2 Ma (Fig. 8) and since exhumation is primarily controlled by denudation, we equate these variations in exhumation with variations in the denudational outflux. According to the model of (Doubrovine and Tarduno, 2008), the plate subduction velocity decreased at ~6 Ma (see Fig. 6b) after an earlier major decrease at ~25 Ma, causing a decrease in the accretionary influx. Conversely, the accretionary influx increased significantly during the Quaternary due to high offshore sedimentation rates and increased sediment thicknesses as a result of effective glacial erosion on the North American continent (e.g. 50–70 % of the present-day sediment thickness on the subducting Juan de Fuca plate consists of Quaternary-aged sediments, Table 1 and Fig. 3).

Hence qualitatively, both influx and outflux vary through time and are particularly affected by the Plio-Pleistocene glaciation, which increased denudation rates and offshore sedimentation rates. However, we cannot quantitatively constrain whether variations in the influx and outflux on these short timescales (2–3 Myr) balance each other (and the system would still be in a flux steady-state). Interestingly, measured denudation rates based on cosmogenic nuclide dating (temporally integrating over the Holocene) suggest, that at present denudation is not affected by glacial erosion, but mostly driven by tectonic rock uplift (Adams and Ehlers, 2018). The Holocene accretionary influx, however, is still affected by the increased sediment thickness since the onset of glaciation. Hence, the current accretionary influx seems to exceed the denudational outflux in the Olympic Mountains.

### 5.4.2 A quantitative perspective

Here, we discuss the quantitative assessment of influx and outflux for the last 14 Myr (Table 5), the time since when the Olympic Mountains are supposed to be in flux steady-state (Batt et al., 2001; Brandon et al., 1998). In the two-dimensional scenario, accretion occurs within a vertical column at the deformation front (Fig. 6a) and exhumation rates are integrated along

a profile across the Olympic Peninsula (Fig. 6d,e). In this scenario, the accretionary influx (~1000 km$^3$) only balances the denudational outflux (1060–1160 km$^3$), if an incoming maximum sediment thickness of 2.5 km is assumed for the 14 Myr

475 period. Although the present-day sediment thickness at the deformation front is ~2.5 km offshore the Olympic Mountains (Fig. 3), the sediment thickness during pre-Quaternary times is difficult to constrain but must have been less (given that at present, 50–70 % of the sediment thickness consists of Quaternary sediments). However, assuming a more realistic scenario, where the sediment thickness increases from 1.5 km to 2.5 km at 2 Ma, yields an accretionary influx of only ~600 km$^3$, which is ~50% of the denudational influx. This suggests, that in a two-dimensional scenario flux steady-state may only be reached, if an

480 unrealistic high sediment thickness is assumed. Alternatively, and more realistic is that the two-dimensional scenario is an oversimplification and the excess in outflux along the considered orogen perpendicular profile may be compensated by an excess of influx at other locations.

In the three-dimensional scenario, accretion occurs not within a vertical column, but along a plane, spanned by the vertical column and the length of the coastline of the Olympic Peninsula, where the elliptic exhumation rate pattern is

485 constrained (Fig. 6a,d). The spatial exhumation rate pattern is integrated to infer the denudational outflux (Fig. 6d). In this scenario, assuming an increase in sediment thickness at 2 Ma yields an accretionary volume (~76,000 km$^3$) close to the denudational outflux (80,000–88,000 km$^3$). Assuming a maximum sediment thickness of 2.5 km for the 14 Myr period yields an accretionary volume of ~130,000 km$^3$, which cannot be reconciled with our denudational outflux (Table 5). Hence, flux steady-state is a plausible assumption over longer timescales (i.e., 14 Myr), if accretion and denudation are considered over

490 large areas (i.e., in three dimensions). This is particularly important in areas like the Olympic Mountains, where exhumation rates are spatially variable.

Sediment volumes integrated along the cross sections (Fig. 7) also provide an interesting perspective on the accretionary influx and denudational outflux in the Olympic Mountains. However, these volumes are not directly comparable with the influx/outflux volumes discussed above (calculated from 14–0 Ma), because the sediment contained within the cross

495 sections (Fig. 7) records accretion since the onset of subduction, which started at ~40 Ma (Brandon et al., 1998; du Bray and John, 2011). Furthermore, these estimates are minimum volumes, because the amount of material that has been eroded during the 40 Myr period is not considered. Nevertheless, the amount of sediment currently residing in the accretionary wedge is variable along strike the subduction zone (1000–5400 km$^3$) and is highest below the central part of the Olympic Mountains (Fig. 7). This requires, that parameters affecting the accretionary influx (like plate subduction velocity or sediment thickness)

500 are highly variable over short distances (e.g. Profile 1 and Profile 2 are only 50 km apart). Another explanation might be, that accretion only perpendicular to the deformation front is an oversimplification and another velocity component also contributes to material transport, so that the location of initial accretion is different from the location of final storage of sediment. This is in accordance with the conclusions drawn above, that considering flux steady-state in a two-dimensional scenario (as it is done with the cross sections) leads to ambiguous results.

505 In summary, the assessment of flux steady state in the Olympic Mountains is non-trivial and many scenarios are possible. From a qualitative viewpoint, flux steady state is probably not achieved on short timescales, because the thickness of

incoming sediment, plate subduction velocity, and exhumation rates show strong temporal variations on timescales of 2–3 Myr. From a quantitative viewpoint, influx and outflux volumes equate each other over longer timescales (i.e., 14 Myr), if influx and outflux are considered in three dimensions. We can only speculate, that margin parallel transport, a contentious

510 mechanism in the Olympic Mountains (Batt et al., 2001; McCrory, 1996), also contributes to the accretionary influx. Present-day GPS velocities corroborate this hypothesis, indicating northward movement of coastal areas south of the Olympic Mountains (e.g. McCaffrey et al., 2013; Wells and McCaffrey, 2013).

**6 Conclusion**

Our new data set of multi-dated thermochronometer bedrock samples together with thermo-kinematic modelling

515 suggests, that several mechanisms contribute to the evolution of the Olympic Mountains. The spatial distribution of reset thermochronometer systems indicates, that the centre of the mountain range has been exhumed from greatest depths. Modelling of the observed AHe, AFT, ZHe, and ZFT ages shows that both variations in the tectonic and climatic parameters result in temporal variations of exhumation rates. The response to the tectonic signal (a reduction in plate convergence rate, causing a drop in exhumation rates) can also be observed in other parts of the Cascadia subduction zone. Plio-Pleistocene glaciation of

520 the Olympic Mountains led to increased denudation, resulting in increased exhumation rates.

Our approach of assessing flux steady-state in the Olympic Mountains by estimating the material influx and outflux independently from each other is promising, but yields ambiguous results. The observed temporal variations in exhumation rate require a variation in the denudational outflux. Likewise, the accretionary influx is also temporally variable, because the plate subduction velocity and incoming sediment thickness are variable through time. Qualitatively, this suggests that flux

525 steady state is perturbed on short timescales. Our quantitative calculations of the influx and outflux show that it is important to consider whether flux steady-state is assessed in two or three dimensions. For the Olympic Mountains, flux steady-state seems to be achieved over long timescales (i.e., 14 Myr), but only, if both influx and outflux are considered in three dimensions.

This study demonstrates the timescale ($10^5$–$10^6$ vs. $10^7$ Myr) and spatial (i.e., two or three dimensional) dependence of a steady-state assessment in an orogenic wedge, an outcome that can also be considered for other mountain ranges.

530 Furthermore, the tremendous effect of the Plio-Pleistocene glaciation is demonstrated, which is capable of significantly perturbing the development of an orogenic wedge, where both the influx (increased offshore sedimentation) and outflux (increased exhumation rates onshore) are affected.

Because the spatial geometry used for assessing flux steady-state is crucial, future work could complement on this and focus on the role of material transport parallel to the deformation front. Further knowledge about this unconstrained

535 parameter would lead to a better understanding of the development of orogenic wedges, situated in a complex tectonic setting like the Olympic Mountains.

**Acknowledgements**

This work was funded by a European Research Council (ERC) Consolidator Grant (615703) to Todd Ehlers. During field work, we had invaluable help and assistance by Holger Sprengel, William Baccus, Jerry Freilich, Roger Hofmann, and the

540 Olympic National Park rangers. We acknowledge Matthias Nettesheim for sharing the code used for evaluation of the tectonic plate reconstruction model.

**References**

Adam, J., Klaeschen, D., Kukowski, N. and Flueh, E.: Upward delamination of Cascadia Basin sediment infill with landward frontal accretion thrusting caused by rapid glacial age material flux, Tectonics, 23(3), doi:10.1029/2002TC001475, 2004.

545

Adams, B. A. and Ehlers, T. A.: Deciphering topographic signals of glaciation and rock uplift in an active orogen: a case study from the Olympic Mountains, USA: Signals of glaciation and rock uplift in the Olympic Mountains, Earth Surface Processes and Landforms, 42(11), 1680–1692, doi:10.1002/esp.4120, 2017.

550 Adams, B. A. and Ehlers, T. A.: Tectonic controls of Holocene erosion in a glaciated orogen, Earth Surf. Dynam., 6(3), 595–610, doi:10.5194/esurf-6-595-2018, 2018.

Adams, B. A., Hodges, K. V., Whipple, K. X., Ehlers, T. A., van Soest, M. C. and Wartho, J.: Constraints on the tectonic and landscape evolution of the Bhutan Himalaya from thermochronometry: Late Cenozoic Evolution of Bhutan, Tectonics, 555 34(6), 1329–1347, doi:10.1002/2015TC003853, 2015.

Batt, G. E., Brandon, M. T., Farley, K. A. and Roden-Tice, M.: Tectonic synthesis of the Olympic Mountains segment of the Cascadia wedge, using two-dimensional thermal and kinematic modeling of thermochronological ages, J. Geophys. Res., 106(B11), 26731–26746, doi:10.1029/2001JB000288, 2001.

560

Bendick, R. and Ehlers, T. A.: Extreme localized exhumation at syntaxes initiated by subduction geometry, Geophys. Res. Lett., 41(16), 2014GL061026, doi:10/f6kfqz, 2014.

Berger, A. L., Gulick, S. P. S., Spotila, J. A., Upton, P., Jaeger, J. M., Chapman, J. B., Worthington, L. A., Pavlis, T. L., 565 Ridgway, K. D., Willems, B. A. and McAleer, R. J.: Quaternary tectonic response to intensified glacial erosion in an orogenic wedge, Nature Geoscience, 1(11), 793–799, doi:10.1038/ngeo334, 2008.

Booth, D. B., Troost, K. G., Clague, J. J. and Waitt, R. B.: The Cordilleran Ice Sheet, in Developments in Quaternary Sciences, vol. 1, pp. 17–43, Elsevier, 2003.

570

Booth-Rea, G., Klaeschen, D., Grevemeyer, I. and Reston, T.: Heterogeneous deformation in the Cascadia convergent margin and its relation to thermal gradient (Washington, NW USA), Tectonics, 27(4), doi:10.1029/2007TC002209, 2008.

Brandon, M. T.: Decomposition of fission-track grain-age distributions, American Journal of Science, 292(8), 535–564, 575 1992.

Brandon, M. T.: Probability density plot for fission-track grain-age sample, Radiation Measurements, 26, 663–676, 1996.

Brandon, M. T. and Calderwood, A. R.: High-pressure metamorphism and uplift of the Olympic subduction complex, 580 Geology, 18(12), 1252, doi:10.1130/0091-7613(1990)018<1252:HPMAUO>2.3.CO;2, 1990.

Brandon, M. T. and Vance, J. A.: Tectonic evolution of the Cenozoic Olympic subduction complex, Washington State, as deduced from fission track ages for detrital zircons, American Journal of Science, 292(8), 565–636, doi:10.2475/ajs.292.8.565, 1992.

585 Brandon, M. T., Roden-Tice, M. K. and Garver, J. I.: Late Cenozoic exhumation of the Cascadia accretionary wedge in the Olympic Mountains, northwest Washington State, Geological Society of America Bulletin, 110(8), 985–1009, doi:10.1130/0016-7606(1998)110<0985:LCEOTC>2.3.CO;2, 1998.

590 Braun, J.: Estimating exhumation rate and relief evolution by spectral analysis of age–elevation datasets, Terra Nova, 14(3), 210–214, 2002.

Braun, J.: Pecube: a new finite-element code to solve the 3D heat transport equation including the effects of a time-varying, finite amplitude surface topography, Computers & Geosciences, 29(6), 787–794, doi:10.1016/S0098-3004(03)00052-9, 595 2003.

du Bray, E. A. and John, D. A.: Petrologic, tectonic, and metallogenic evolution of the Ancestral Cascades magmatic arc, Washington, Oregon, and northern California, Geosphere, 7(5), 1102–1133, 2011.

600 Calvert, A. J., Preston, L. A. and Farahbod, A. M.: Sedimentary underplating at the Cascadia mantle-wedge corner revealed by seismic imaging, Nature Geosci., 4(8), 545–548, doi:10.1038/ngeo1195, 2011.

Carpentier, M., Weis, D. and Chauvel, C.: Fractionation of Sr and Hf isotopes by mineral sorting in Cascadia Basin terrigenous sediments, Chemical Geology, 382, 67–82, doi:10.1016/j.chemgeo.2014.05.028, 2014.
605
Clague, J. J. and James, T. S.: History and isostatic effects of the last ice sheet in southern British Columbia, Quaternary Science Reviews, 21(1), 71–87, 2002.

Clowes, R. M., Brandon, M. T., Green, A. G., Yorath, C. J., Brown, A. S., Kanasewich, E. R. and Spencer, C.: 610 LITHOPROBE-southern Vancouver Island: Cenozoic subduction complex imaged by deep seismic reflections, Canadian Journal of Earth Sciences, 24(1), 31–51, 1987.

Davis, E. E. and Hyndman, R. D.: Accretion and recent deformation of sediments along the northern Cascadia subduction zone, Geological Society of America Bulletin, 101(11), 1465–1480, 1989.
615
Doubrovine, P. V. and Tarduno, J. A.: A revised kinematic model for the relative motion between Pacific oceanic plates and North America since the Late Cretaceous, Journal of Geophysical Research, 113(B12), doi:10.1029/2008JB005585, 2008.

Easterbrook, D. J.: Stratigraphy and chronology of quaternary deposits of the Puget Lowland and Olympic Mountains of 620 Washington and the Cascade Mountains of Washington and Oregon, Quaternary Science Reviews, 5, 145–159, doi:10.1016/0277-3791(86)90180-0, 1986.

Eddy, M. P., Clark, K. P. and Polenz, M.: Age and volcanic stratigraphy of the Eocene Siletzia oceanic plateau in Washington and on Vancouver Island, Lithosphere, 9(4), 652–664, doi:10.1130/L650.1, 2017.
625
Ehlers, T. A.: Computational Tools for Low-Temperature Thermochronometer Interpretation, Reviews in Mineralogy and Geochemistry, 58(1), 589–622, doi:10.2138/rmg.2005.58.22, 2005.

Ehlers, T. A., Farley, K. A., Rusmore, M. E. and Woodsworth, G. J.: Apatite (U-Th)/He signal of large-magnitude 630 accelerated glacial erosion, southwest British Columbia, Geology, 34(9), 765, doi:10.1130/G22507.1, 2006.

Falkowski, S. and Enkelmann, E.: Upper-crustal cooling of the Wrangellia composite terrane in the northern St. Elias Mountains, western Canada, Lithosphere, 8(4), 359–378, doi:10.1130/L508.1, 2016.

635 Falkowski, S., Enkelmann, E. and Ehlers, T. A.: Constraining the area of rapid and deep-seated exhumation at the St. Elias syntaxis, Southeast Alaska, with detrital zircon fission-track analysis, Tectonics, 33(5), 597–616, doi:10.1002/2013TC003408, 2014.

Farley, K. A.: (U-Th)/He Dating: Techniques, Calibrations, and Applications, Reviews in Mineralogy and Geochemistry, 640 47(1), 819–844, doi:10.2138/rmg.2002.47.18, 2002.

Fitzgerald, P. G., Stump, E. and Redfield, T. F.: Late Cenozoic uplift of Denali and its relation to relative plate motion and fault morphology, Science, 259, 497–497, 1993.

645 Flueh, E. R., Fisher, M. A., Bialas, J., Childs, J. R., Klaeschen, D., Kukowski, N., Parsons, T., Scholl, D. W., ten Brink, U. and Tréhu, A. M.: New seismic images of the Cascadia subduction zone from cruise SO108—ORWELL, Tectonophysics, 293(1), 69–84, 1998.

Galbraith, R. F.: Statistics for fission track analysis, CRC Press., 2005.
650
Glotzbach, C., van der Beek, P., Carcaillet, J. and Delunel, R.: Deciphering the driving forces of erosion rates on millennial to million-year timescales in glacially impacted landscapes: An example from the Western Alps, Journal of Geophysical Research: Earth Surface, 118(3), 1491–1515, doi:10.1002/jgrf.20107, 2013.

655 Gulick, S. P. S., Jaeger, J. M., Mix, A. C., Asahi, H., Bahlburg, H., Belanger, C. L., Berbel, G. B. B., Childress, L., Cowan, E., Drab, L., Forwick, M., Fukumura, A., Ge, S., Gupta, S., Kioka, A., Konno, S., LeVay, L. J., März, C., Matsuzaki, K. M., McClymont, E. L., Moy, C., Müller, J., Nakamura, A., Ojima, T., Ribeiro, F. R., Ridgway, K. D., Romero, O. E., Slagle, A. L., Stoner, J. S., St-Onge, G., Suto, I., Walczak, M. D., Worthington, L. L., Bailey, I., Enkelmann, E., Reece, R. and Swartz, J. M.: Mid-Pleistocene climate transition drives net mass loss from rapidly uplifting St. Elias Mountains, Alaska, 660 Proceedings of the National Academy of Sciences, 112(49), 15042–15047, doi:10.1073/pnas.1512549112, 2015.

Gutscher, M.-A., Klaeschen, D., Flueh, E. and Malavieille, J.: Non-Coulomb wedges, wrong-way thrusting, and natural hazards in Cascadia, Geology, 29(5), 379–382, 2001.

665 Han, S., Carbotte, S. M., Canales, J. P., Nedimović, M. R., Carton, H., Gibson, J. C. and Horning, G. W.: Seismic reflection imaging of the Juan de Fuca plate from ridge to trench: New constraints on the distribution of faulting and evolution of the crust prior to subduction, Journal of Geophysical Research: Solid Earth, 121(3), 1849–1872, doi:10.1002/2015JB012416, 2016.

670 Haug, G. H., Ganopolski, A., Sigman, D. M., Rosell-Mele, A. and others: North Pacific seasonality and the glaciation of North America 2.7 million years ago, Nature, 433(7028), 821, 2005.

Hayes, G. P., Wald, D. J. and Johnson, R. L.: Slab1.0: A three-dimensional model of global subduction zone geometries:, Journal of Geophysical Research: Solid Earth, 117(B1), doi:10.1029/2011JB008524, 2012.
675
Herman, F. and Brandon, M.: Mid-latitude glacial erosion hotspot related to equatorial shifts in southern Westerlies, Geology, 43(11), 987–990, doi:10.1130/G37008.1, 2015.

Herman, F., Seward, D., Valla, P. G., Carter, A., Kohn, B., Willett, S. D. and Ehlers, T. A.: Worldwide acceleration of 680 mountain erosion under a cooling climate, Nature, 504(7480), 423–426, doi:10.1038/nature12877, 2013.

Hourigan, J. K., Reiners, P. W. and Brandon, M. T.: U-Th zonation-dependent alpha-ejection in (U-Th)/He chronometry, Geochimica et Cosmochimica Acta, 69(13), 3349–3365, doi:10.1016/j.gca.2005.01.024, 2005.

685 Hurford, A. J.: Standardization of fission track dating calibration: Recommendation by the Fission Track Working Group of the I.U.G.S. Subcommission on Geochronology, Chemical Geology, 80, 171–178, 1990.

Hyndman, R. D. and Wang, K.: Thermal constraints on the zone of major thrust earthquake failure: The Cascadia Subduction Zone, Journal of Geophysical Research: Solid Earth, 98(B2), 2039–2060, doi:10.1029/92JB02279, 1993.

690 Hyndman, R. D., Yorath, C. J., Clowes, R. M. and Davis, E. E.: The northern Cascadia subduction zone at Vancouver Island: Seismic structure and tectonic history, Canadian Journal of Earth Sciences, 27(3), 313–329, 1990.

Kiyokawa, S. and Yokoyama, K.: Provenance of turbidite sands from IODP EXP 1301 in the northwestern Cascadia Basin, 695 western North America, Marine Geology, 260(1–4), 19–29, doi:10.1016/j.margeo.2009.01.003, 2009.

Knudson, K. P. and Hendy, I. L.: Climatic influences on sediment deposition and turbidite frequency in the Nitinat Fan, British Columbia, Marine Geology, 262(1–4), 29–38, doi:10.1016/j.margeo.2009.03.002, 2009.

700 Kulm, L. V. D., von Huene, R., Duncan, J. R., Ingle, J. C., Kling, S. A., Musich, L. F., Piper, D. J. W., Pratt, R. M., Schrader, H.-J., Weser, O. E. and Wise, S. W.: Site 174, edited by L. V. D. Kulm, R. von Huene, J. R. Duncan, J. C. Ingle, S. A. Kling, D. J. W. Piper, R. M. Pratt, H.-J. Schrader, S. W. Wise, L. F. Musich, and O. E. Weser, Initial Reports of the Deep Sea Drilling Project, 18, 97, 1973.

705 Lease, R. O. and Ehlers, T. A.: Incision into the Eastern Andean Plateau During Pliocene Cooling, Science, 341(6147), 774–776, doi:10.1126/science.1239132, 2013.

Lease, R. O., Haeussler, P. J. and O'Sullivan, P.: Changing exhumation patterns during Cenozoic growth and glaciation of the Alaska Range: Insights from detrital thermochronology and geochronology, Tectonics, 35(4), 934–955, 710 doi:10.1002/2015TC004067, 2016.

Leeman, W. P., Lewis, J. F., Evarts, R. C., Conrey, R. M. and Streck, M. J.: Petrologic constraints on the thermal structure of the Cascades arc, Journal of Volcanology and Geothermal Research, 140(1–3), 67–105, doi:10.1016/j.jvolgeores.2004.07.016, 2005.
715
Lewis, T. J. and Bentkowski, W. H.: Potassium, Uranium and Thorium Concentrations of Crustal Rocks: a Data File, Open File Report 1744, Geological Survey of Canada, Sidney, 1988.

Lewis, T. J., Bentkowski, W. H., Davis, E. E., Hyndman, R. D., Souther, J. G. and Wright, J. A.: Subduction of the Juan de 720 Fuca Plate: Thermal consequences, Journal of Geophysical Research: Solid Earth, 93(B12), 15207–15225, doi:10.1029/JB093iB12p15207, 1988.

McCaffrey, R., King, R. W., Payne, S. J. and Lancaster, M.: Active tectonics of northwestern U.S. inferred from GPS-derived surface velocities, Journal of Geophysical Research: Solid Earth, 118(2), 709–723, doi:10.1029/2012JB009473, 725 2013.

McCrory, P. A.: Tectonic model explaining divergent contraction directions along the Cascadia subduction margin, Washington, Geology, 24(10), 929, doi:10.1130/0091-7613(1996)024<0929:TMEDCD>2.3.CO;2, 1996.

730    McCrory, P. A., Blair, J. L., Waldhauser, F. and Oppenheimer, D. H.: Juan de Fuca slab geometry and its relation to Wadati-Benioff zone seismicity, Journal of Geophysical Research: Solid Earth, 117(B9), doi:10.1029/2012JB009407, 2012.

       McNeill, L. C., Goldfinger, C., Kulm, L. D. and Yeats, R. S.: Tectonics of the Neogene Cascadia forearc basin: Investigations of a deformed late Miocene unconformity, Geological Society of America Bulletin, 112(8), 1209–1224, 2000.

735
       Meesters, A. G. C. A. and Dunai, T. J.: A noniterative solution of the (U-Th)/He age equation, Geochemistry, Geophysics, Geosystems, 6(4), doi:10.1029/2004GC000834, 2005.

       Michel, L., Ehlers, T. A., Glotzbach, C., Adams, B. A. and Stübner, K.: Tectonic and glacial contributions to focused
740    exhumation in the Olympic Mountains, Washington, USA, Geology, 46(6), 491–494, doi:10/gc8z9w, 2018.

       Montgomery, D. R.: Valley formation by fluvial and glacial erosion, Geology, 30(11), 1047–1050, doi:10.1130/0091-7613(2002)030<1047:VFBFAG>2.0.CO;2, 2002.

745    Montgomery, D. R. and Greenberg, H. M.: Local relief and the height of Mount Olympus, Earth Surface Processes and Landforms, 25(4), 385–396, 2000.

       Mullen, E. K., Weis, D., Marsh, N. B. and Martindale, M.: Primitive arc magma diversity: New geochemical insights in the Cascade Arc, Chemical Geology, 448, 43–70, doi:10.1016/j.chemgeo.2016.11.006, 2017.
750
       Mutz, S. G., Ehlers, T. A., Werner, M., Lohmann, G., Stepanek, C. and Li, J.: Estimates of late Cenozoic climate change relevant to Earth surface processes in tectonically active orogens, Earth Surface Dynamics, 6(2), 271–301, doi:10/gc8sbw, 2018.

755    Phillips, B. A., Kerr, A. C., Mullen, E. K. and Weis, D.: Oceanic mafic magmatism in the Siletz terrane, NW North America: Fragments of an Eocene oceanic plateau?, Lithos, 274–275, 291–303, doi:10.1016/j.lithos.2017.01.005, 2017.

       Porter, S. C.: Composite Pleistocene snow line of Olympic Mountains and Cascade Range, Washington, Geological Society of America Bulletin, 75(5), 477–482, 1964.
760
       Priest, G. R.: Volcanic and tectonic evolution of the Cascade Volcanic Arc, central Oregon, Journal of Geophysical Research: Solid Earth, 95(B12), 19583–19599, doi:10.1029/JB095iB12p19583, 1990.

       Prytulak, J., Vervoort, J. D., Plank, T. and Yu, C.: Astoria Fan sediments, DSDP site 174, Cascadia Basin: Hf–Nd–Pb
765    constraints on provenance and outburst flooding, Chemical Geology, 233(3–4), 276–292, doi:10.1016/j.chemgeo.2006.03.009, 2006.

       Reiners, P. W., Zhou, Z., Ehlers, T. A., Xu, C., Brandon, M. T., Donelick, R. A. and Nicolescu, S.: Post-orogenic evolution of the Dabie Shan, eastern China, from (U-Th)/He and fission-track thermochronology, American Journal of Science,
770    303(6), 489–518, 2003.

       Stewart, R. J. and Brandon, M. T.: Detrital-zircon fission-track ages for the "Hoh Formation": implications for late Cenozoic evolution of the Cascadia subduction wedge, Geological Society of America Bulletin, 116(1–2), 60–75, 2004.

775    Stolar, D., Roe, G. and Willett, S.: Controls on the patterns of topography and erosion rate in a critical orogen, Journal of Geophysical Research, 112(F4), doi:10.1029/2006JF000713, 2007.

Stübner, K., Drost, K., Schoenberg, R., Böhme, M., Starke, J. and Ehlers, T. A.: Asynchronous timing of extension and basin
formation in the South Rhodope core complex, SW Bulgaria, and northern Greece, Tectonics, 35(1), 136–159,
780    doi:10.1002/2015TC004044, 2016.

Su, X., Baumann, K. H. and Thiede, J.: Calcareous nannofossils from Leg 168: biochronology and diagenesis, in
Proceedings of the Ocean Drilling Program, Scientific Results, vol. 168, pp. 39–50., 2000.

785    Tabor, R. W. and Cady, W. M.: The structure of the Olympic Mountains, Washington: Analysis of a subduction zone, US
Govt. Print. Off., 1978.

Thackray, G. D.: Extensive Early and Middle Wisconsin Glaciation on the Western Olympic Peninsula, Washington, and the
Variability of Pacific Moisture Delivery to the Northwestern United States, Quaternary Research, 55(3), 257–270,
790    doi:10.1006/qres.2001.2220, 2001.

Thiede, R. C. and Ehlers, T. A.: Large spatial and temporal variations in Himalayan denudation, Earth and Planetary Science
Letters, 371–372, 278–293, doi:10.1016/j.epsl.2013.03.004, 2013.

795    Thomson, S. N., Brandon, M. T., Tomkin, J. H., Reiners, P. W., Vásquez, C. and Wilson, N. J.: Glaciation as a destructive
and constructive control on mountain building, Nature, 467(7313), 313–317, doi:10.1038/nature09365, 2010.

Tomkin, J. H. and Roe, G. H.: Climate and tectonic controls on glaciated critical-taper orogens, Earth and Planetary Science
Letters, 262(3–4), 385–397, doi:10.1016/j.epsl.2007.07.040, 2007.
800
Valla, P. G., Shuster, D. L. and van der Beek, P. A.: Significant increase in relief of the European Alps during mid-
Pleistocene glaciations, Nature Geosci, 4(10), 688–692, doi:10.1038/ngeo1242, 2011.

Wells, R. E. and McCaffrey, R.: Steady rotation of the Cascade arc, Geology, 41(9), 1027–1030, doi:10.1130/G34514.1,
805    2013.

Wells, R. E., Bukry, D., Friedman, R., Pyle, D., Duncan, R., Haeussler, P. and Wooden, J.: Geologic history of Siletzia, a
large igneous province in the Oregon and Washington Coast Range: Correlation to the geomagnetic polarity time scale and
implications for a long-lived Yellowstone hotspot, Geosphere, 10(4), 692–719, 2014.
810
Westbrook, G., Carson, B. and Musgrave, R.: Shipboard Scientific Party, 1994, Initial reports of the Ocean Drilling
Program, 146(pt 1), 1994.

Whipple, K. X.: The influence of climate on the tectonic evolution of mountain belts, Nature Geosci., 2(2), 97–104,
815    doi:10.1038/ngeo413, 2009.

Whipple, K. X. and Meade, B.: Orogen response to changes in climatic and tectonic forcing, Earth and Planetary Science
Letters, 243(1–2), 218–228, doi:10.1016/j.epsl.2005.12.022, 2006.

820    Willett, S. D.: Orogeny and orography: The effects of erosion on the structure of mountain belts, J. Geophys. Res., 104(B12),
28957–28981, doi:10.1029/1999JB900248, 1999.

Willett, S. D. and Brandon, M. T.: On steady states in mountain belts, Geology, 30(2), 175–178, doi:10.1130/0091-
7613(2002)030<0175:OSSIMB>2.0.CO;2, 2002.
825
Wilson, D. S.: Confidence intervals for motion and deformation of the Juan de Fuca Plate, Journal of Geophysical Research:
Solid Earth, 98(B9), 16053–16071, doi:10.1029/93JB01227, 1993.

Wilson, D. S.: The Juan de Fuca plate and slab: Isochron structure and Cenozoic plate motions, in: The Cascadia Subduction
830    Zone and related subduction systems: seismic structure, intraslab earthquakes and processes, and earthquake hazards, US
Geological Survey, Reston, VA., 2002.

Yuan, T., Spence, G. D. and Hyndman, R. D.: Seismic velocities and inferred porosities in the accretionary wedge sediments
at the Cascadia margin, Journal of Geophysical Research: Solid Earth, 99(B3), 4413–4427, doi:10/dfwxqf, 1994.
835
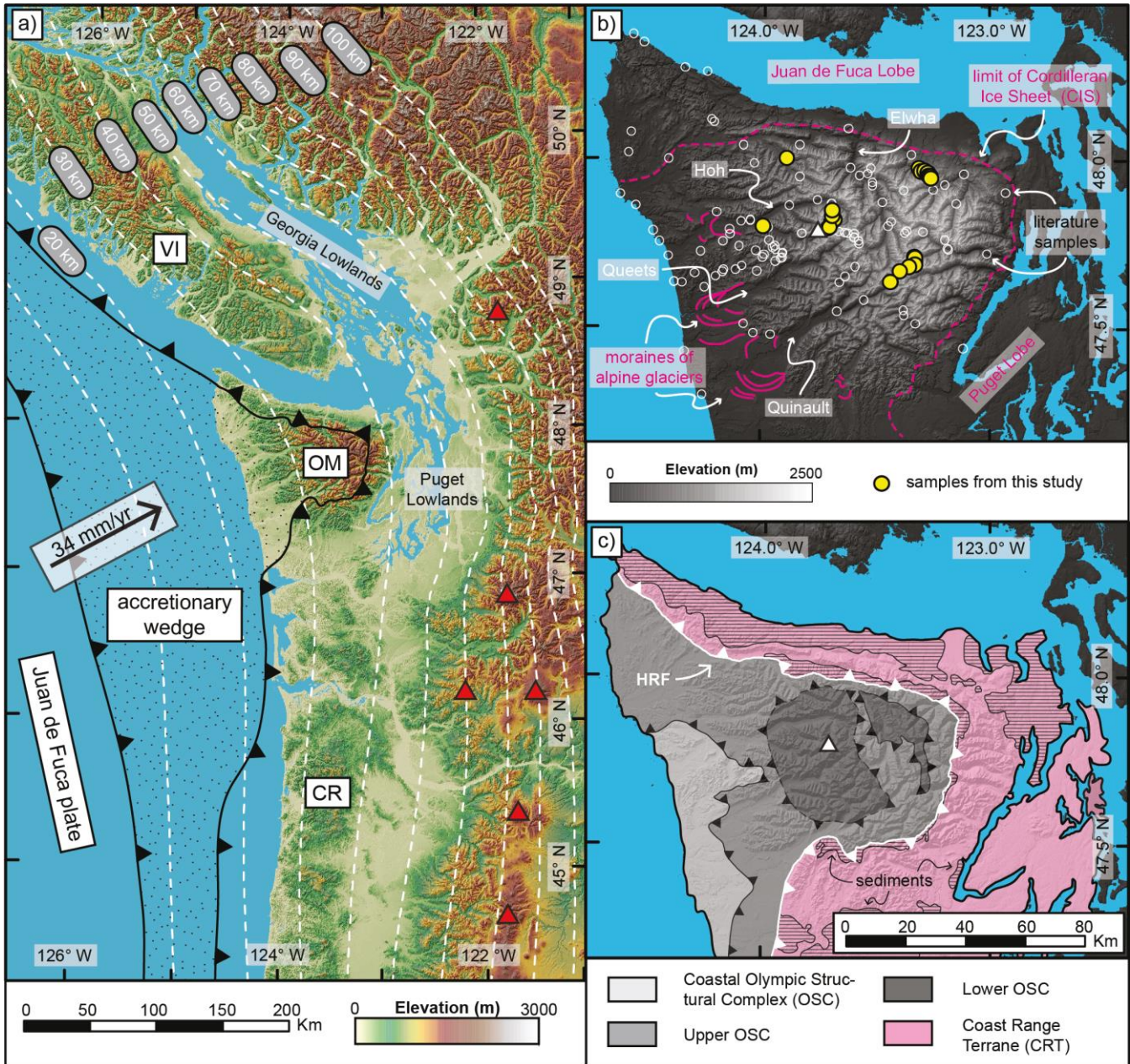
**Figure 1: a**) Overview map of the Cascadia subduction zone, showing the extent of the accretionary wedge. White dashed lines are contour lines for the top of the subducted oceanic plate from the Slab1.0 model (Hayes et al., 2012; McCrory et al., 2012), the black arrow indicates the present-day convergence rate and direction at the latitude of the Olympics (Doubrovine and Tarduno, 2008), red triangles denote the location of active volcanoes. VI = Vancouver Island, OM = Olympic Mountains, CR = Oregon Coast Range. **b**) Topography of the Olympic Mountains, major river valleys (Elwha, Hoh, Quinault, Queets) and major Quaternary features are indicated. Limit of the Cordilleran Ice Sheet from Porter (1964), alpine moraines after geologic map of Tabor and Cady, (1978). Locations of samples from this study (filled yellow circles) and previous studies (open white circles) are indicated. The white triangle denotes the location of Mt. Olympus. **c**) Geologic and structural map of the Olympic Mountains after Tabor and Cady (1978) and Brandon et al. (1998). The line pattern indicates the occurrence of sediments within the Coast Range Terrane. HRF = Hurricane Ridge Fault.
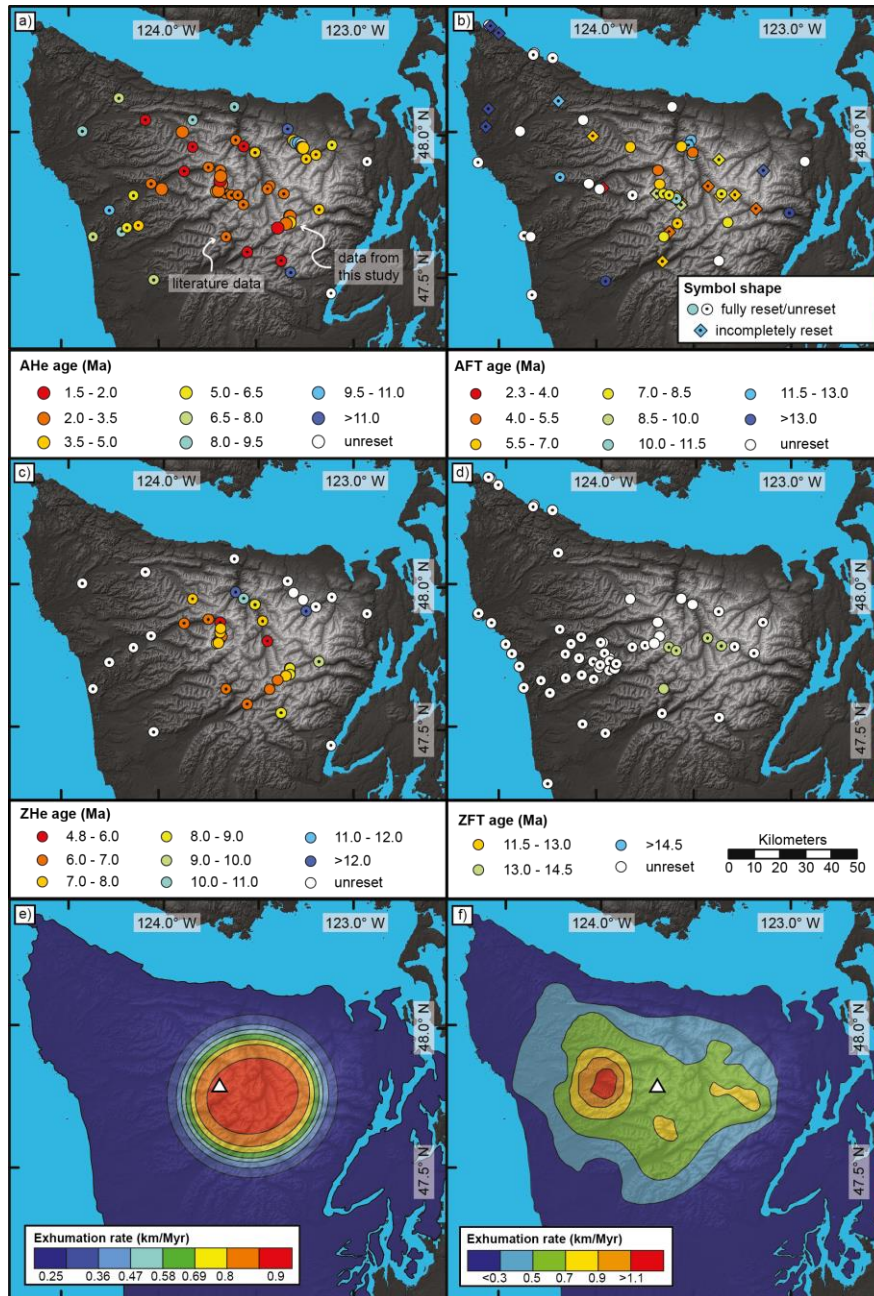
**Figure 2:** Map of new and previous thermochronometric ages within the Olympic Mountains for a) AHe, b) AFT, c) ZHe and d) ZFT. Data from literature sources (Batt et al., 2001; Brandon et al., 1998; Brandon and Vance, 1992; Michel et al., 2018; Stewart and Brandon, 2004) are indicated by symbols containing a black dot. Note that the colour coding of the symbols is variable from subpanel to subpanel. For AFT literature samples, the different reset state (fully reset, incompletely reset and unreset) is indicated by symbol shape. Brandon et al. (1998) discern the incompletely reset AFT samples also in partially and multiply reset samples (based on the grain age peaks of the respective sample). However, for our purpose it is enough to know whether samples are reset or unreset (i.e., we treat incompletely reset samples as unreset samples due to our modelling approach). Maps of exhumation rates suggested by e) Michel et al. (2018) based on AHe and ZHe ages and f) Brandon et al. (1998) based on their AFT ages. The white triangle denotes the location of Mt. Olympus.
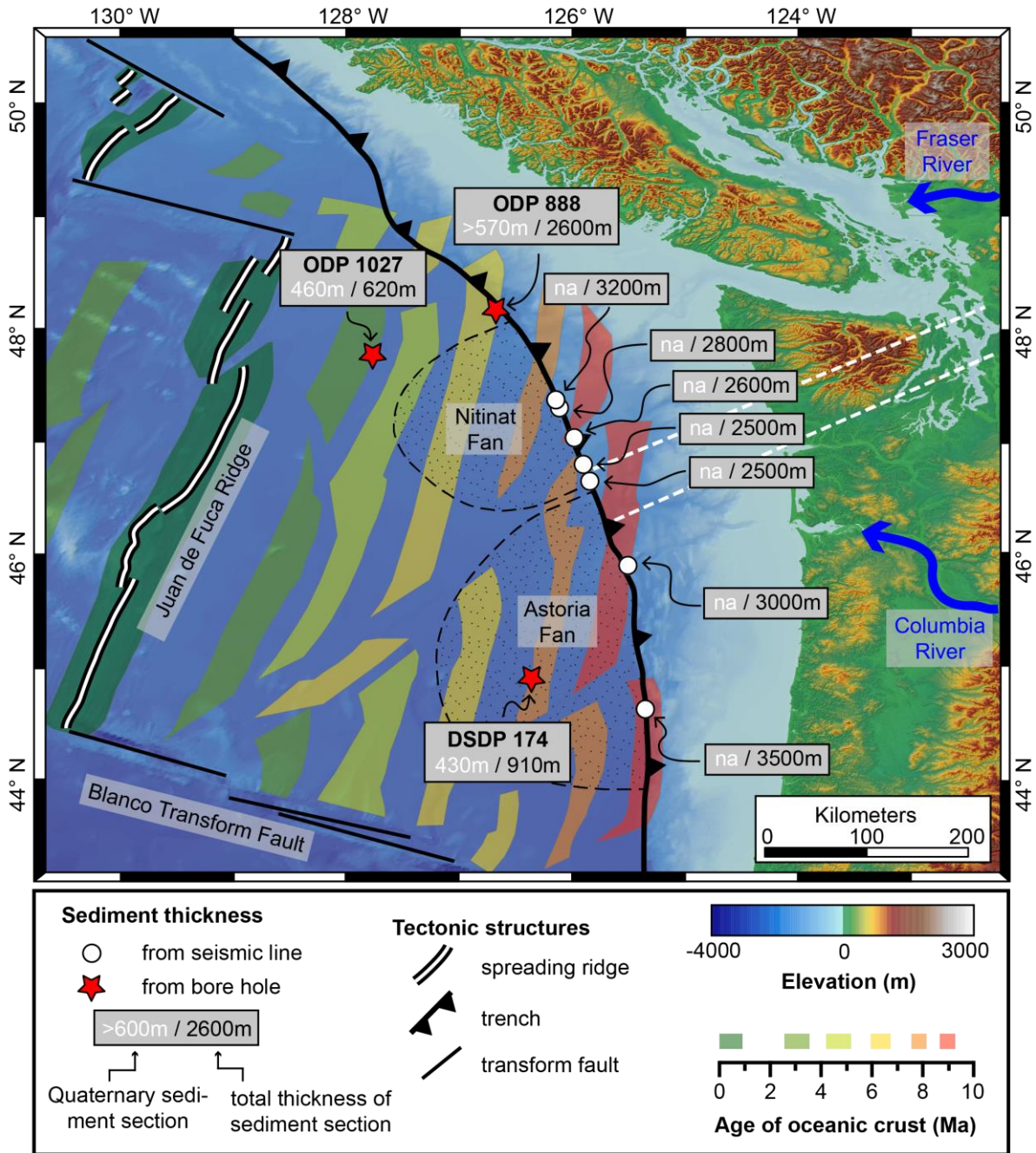
**Figure 3:** Map of the Cascadia subduction zone, showing the age of the oceanic crust (Wilson, 1993) and sediment thickness, estimated
from sediment cores of the ocean drilling programs (holes ODP 888, OPD 1027 and DSDP 174) and seismic studies (Adam et al., 2004;
Booth-Rea et al., 2008; Han et al., 2016). For the cores, the amount of Quaternary sediment material is given as well (Kulm et al., 1973; Su
et al., 2000; Westbrook et al., 1994), more information about the drill cores is provided in Table 1. The location of two major submarine
fans (Nitinat Fan and Astoria Fan) is indicated by the dotted pattern. The Fraser and Columbia rivers are the main modern sediment sources
for Nitinat and Astoria fans, respectively. White, dashed lines indicate the position of cross sections presented in this study (Fig. 7).

865
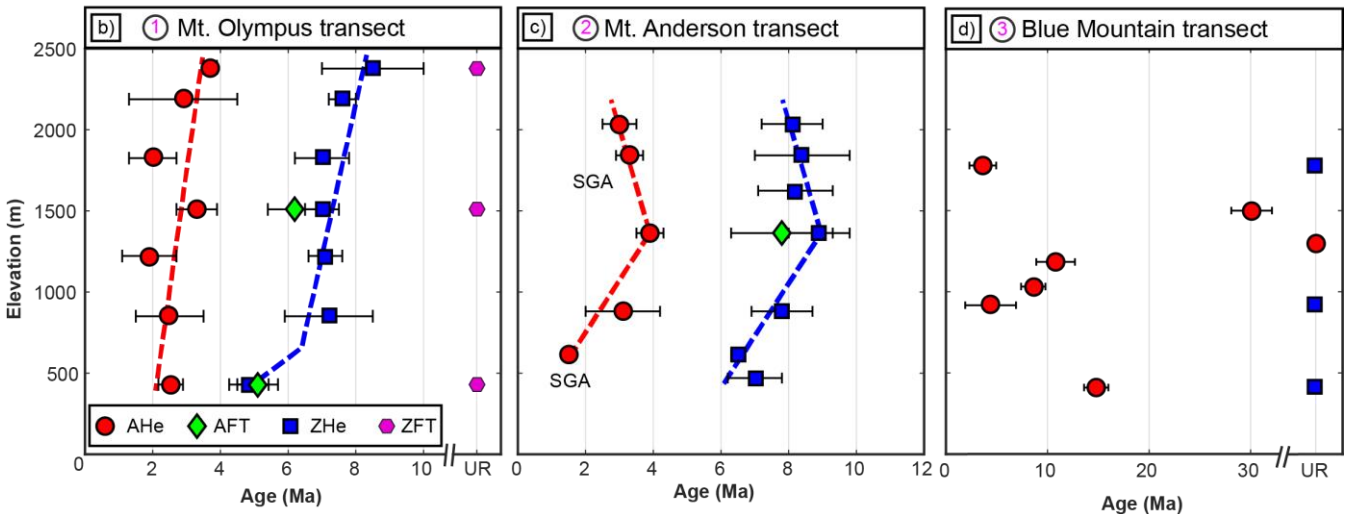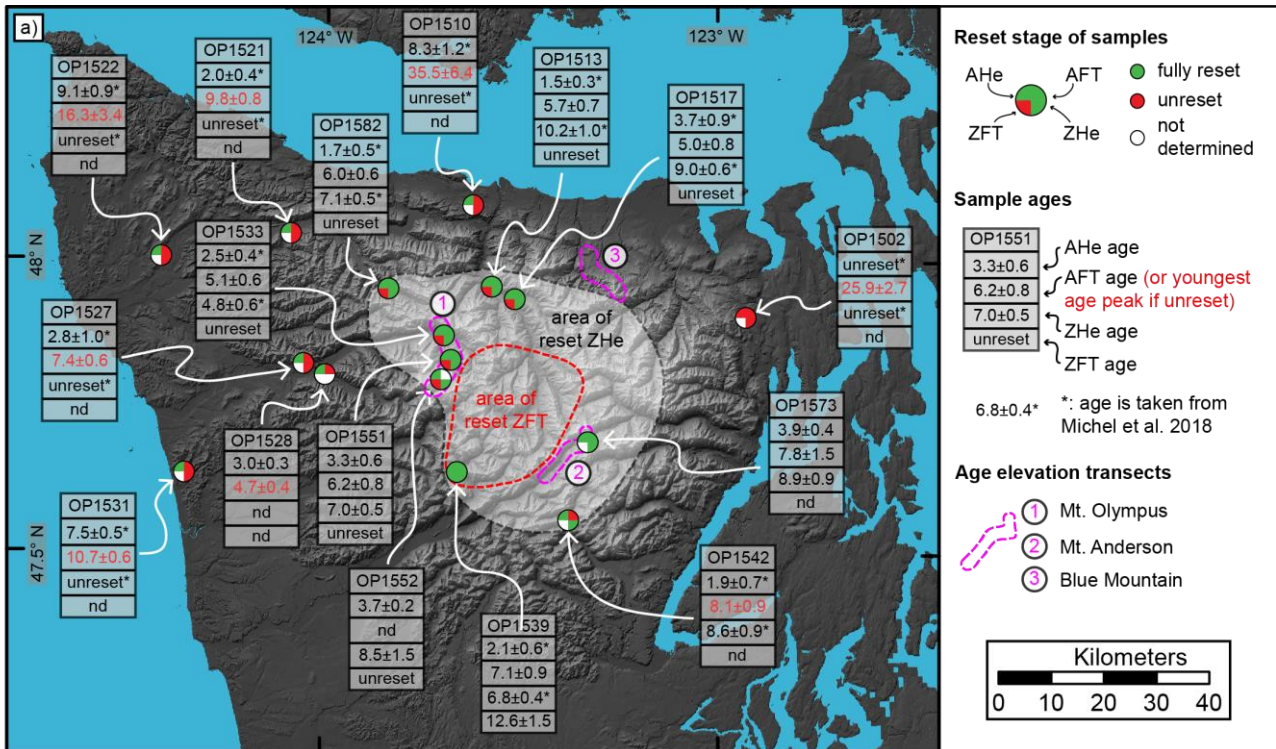
**Figure 4:** a) Map of samples, for which three to four different thermochronometer systems are available. The pie charts allow for easy identification of the reset stage of a particular thermochronometer system for the respective sample. If AFT ages are unreset, the peak age of the youngest age population is given as age (see Table 3 for older peak ages). Ages denoted with an asterisk are taken from Michel et al. (2018). The location of the three different age elevation transects (Mt. Olympus, Mt. Anderson and Blue Mountain) is indicated on the map

870   and the resulting age elevation plots are shown in subpanels b) to d). In b) and c) the dashed coloured lines correspond to possible exhumation rates interpreted from the respective thermochronometer. All uncertainties are 1 standard deviation, SGA = single-grain age.
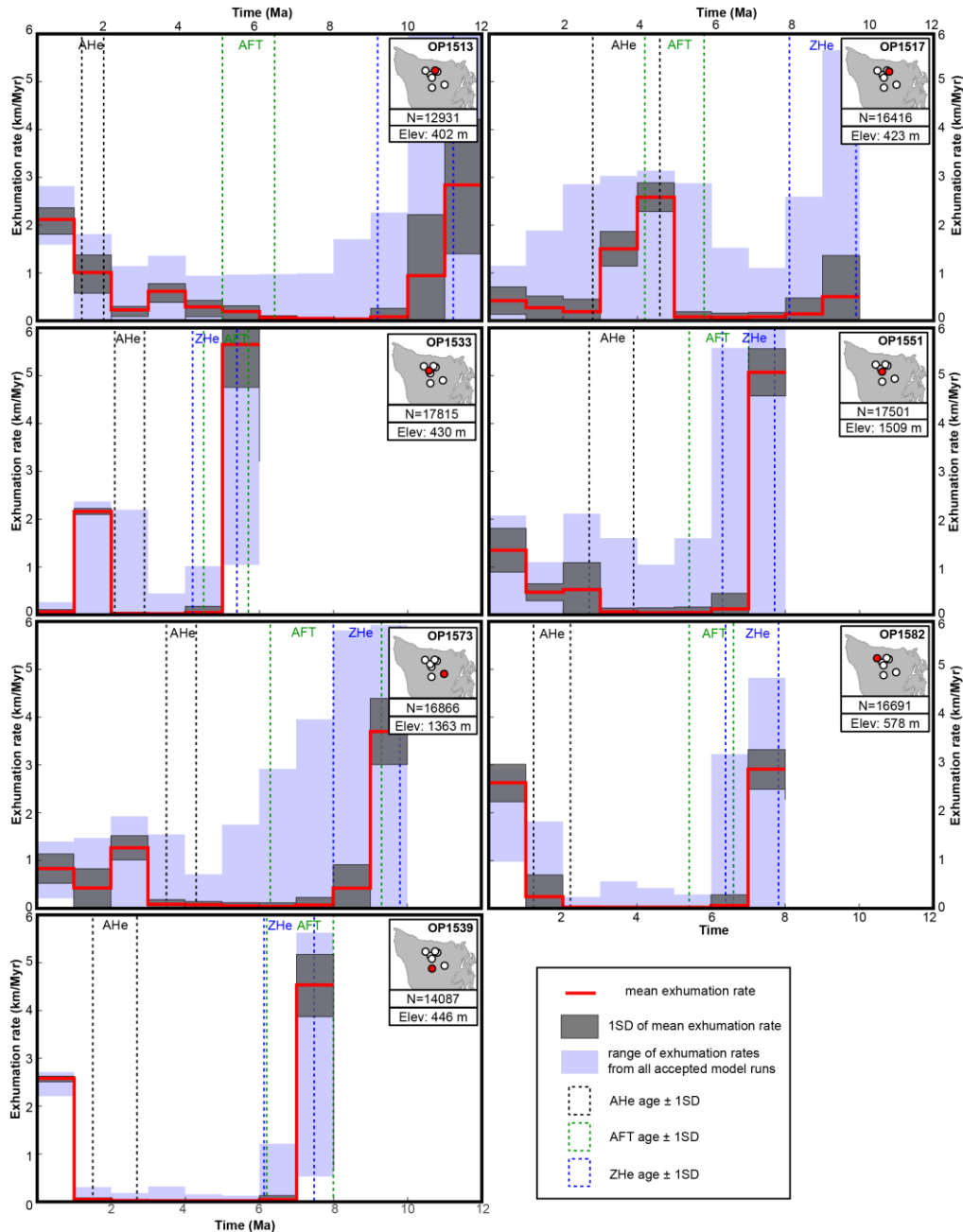
**Figure 5:** Results from the thermo-kinematic Monte Carlo modelling for the seven considered samples (OP1513, OP1517, OP1533, OP1539, OP1551, OP1573, OP1582). Location of the respective sample within the Olympic Peninsula is shown, together with the respective elevation (Elev). The entire range of the exhumation rate from the number of accepted model runs (N) is outlined by the blue shaded area, from which the mean rate and one standard deviation (1SD) is calculated at each time step. Black, green and blue stippled boxes outline measured AHe, AFT and ZHe ages of the samples with 1SD.
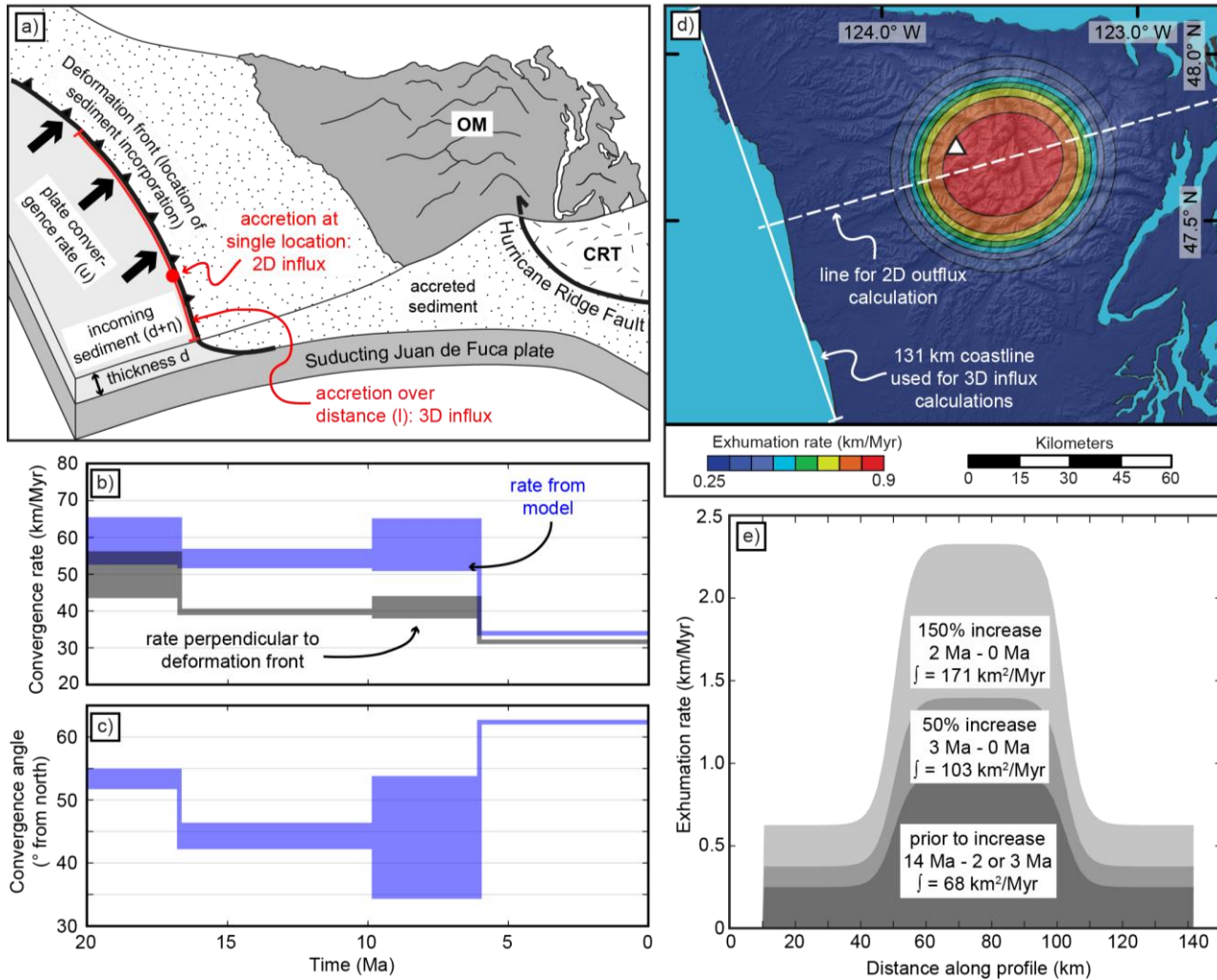
**Figure 6:** Constraints used for our quantitative accretionary influx and denudational outflux calculations: a) Cartoon illustrating our approach for calculating the accretionary influx. The influx corresponds to the sediment off-scraped from the subducting Juan de Fuca Plate, and is governed by the plate convergence rate (u) and the incoming sediment properties (thickness d, porosity η). We discern a two-dimensional scenario, where sediment is accreted at a single location within a vertical column at the deformation front, and a three-dimensional scenario, where accretion is considered along a length (l) within a vertical plane. OM = Olympic Mountains, CRT = Coast Range Terrane. b) Temporal evolution of the plate convergence rate used in our calculations, considering only the component perpendicular to the deformation front (black envelope), and the original output (blue envelope) from the plate reconstruction model of Doubrovine and Tarduno (2008). To provide an uncertainty for our calculations, we consider a range of convergence rates (comprising the width of the envelope) for each time step, based on two different rotation models in the model of Doubrovine and Tarduno (2008) (see text for details). c) Temporal evolution of the plate convergence angle (Doubrovine and Tarduno, 2008) used to correct the plate convergence rate in b). d) Exhumation rate pattern from Michel et al. (2018) used for our outflux calculations. The range of displayed rates (0.25–0.9 km/Ma) corresponds to the rates prior to the glacially induced increase in exhumation rates. In the two-dimensional scenario, we integrate the exhumation rates along the dashed line (displayed in panel e). In the three-dimensional scenario, we integrate over the entire pattern. e) Exhumation rates along the line shown in panel d) and the resulting value of the integral, prior to the glacially induced increase in rates, for a 50% increase and a 150% increase. The duration over which the respective integral is applied is indicated as well.
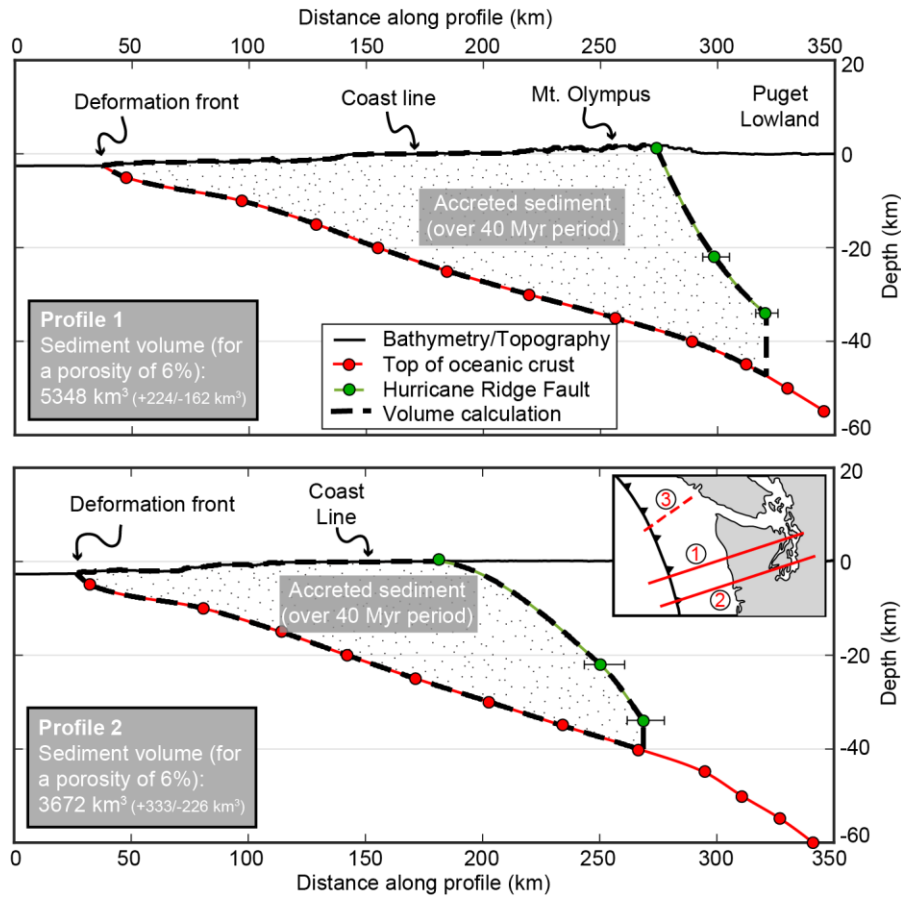
**Figure 7:** Sediment volumes calculated along two cross sections spanning the Olympic Peninsula (Profile 1 and 2, vertical exaggeration=2, see inset for location). For explanation of the used procedure see text. The reported uncertainties for the volume are based on the uncertainties in the position of the Hurricane Ridge Fault (indicated with error bars at the respective symbol). Numbers in inset correspond to (1) = position of Profile 1, (2) = position of Profile 2, (3) = position of profile by Davis and Hyndman (1989), referred to in the text.

900
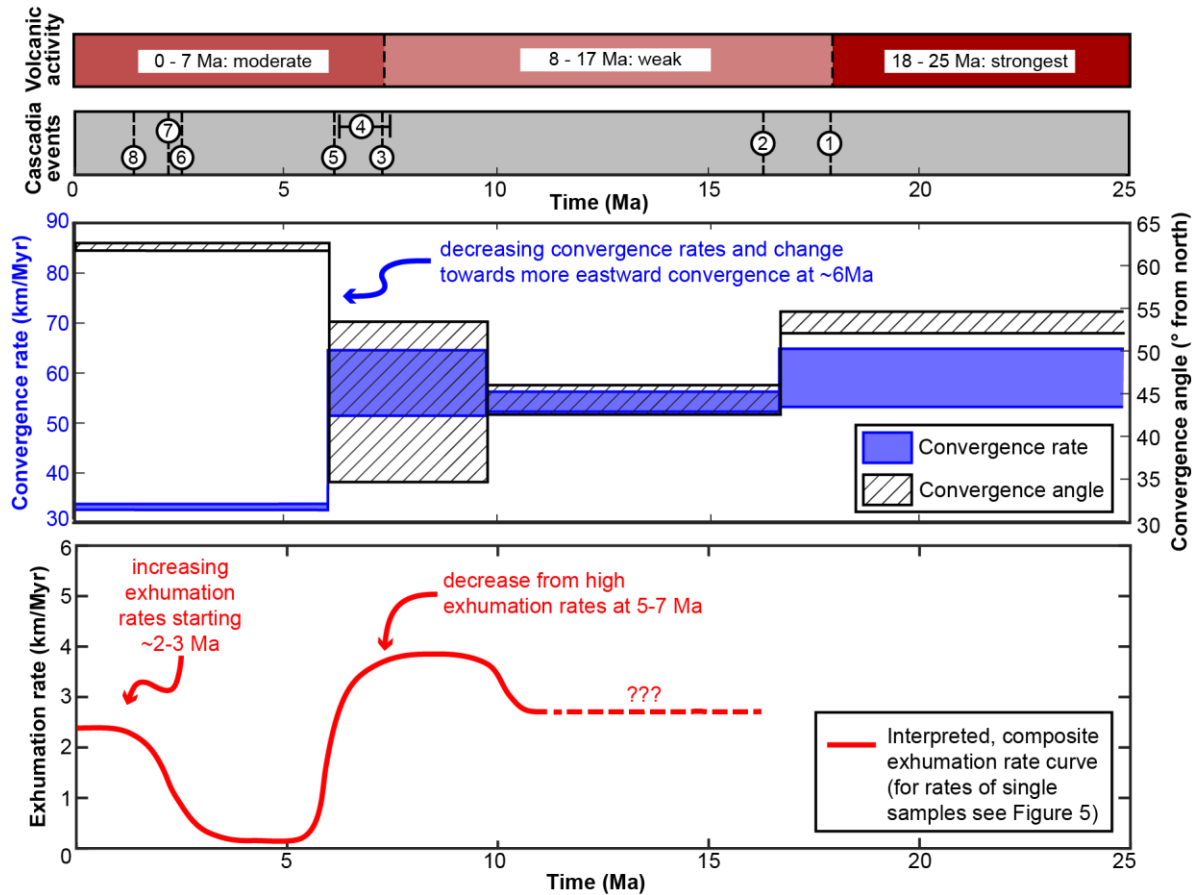
**Figure 8:** Summary of volcanic activity, tectonic and climatic events, convergence rate and angle at the Cascadia Subduction zone compared to our modelled exhumation rates for the past 25 Ma. Exhumation rates are limited to the time interval covered by our thermochronometric ages (11–0 Ma). The curve depicts the interpreted evolution of exhumation rates, based on the modelling results shown in Fig. 5. See text for details. Volcanic activity after du Bray and John (2011). Tectonic and climatic events are (1) start of exhumation of the Olympics (Brandon et al. 1998), (2) onset of uplift of the Oregon Coast Range (McNeill et al., 2000), (3) rotation in stress field (Priest, 1990), (4) faster uplift in Oregon Coast Range (McNeill et al., 2000), (5) Pacific wide plate reorganization (Wilson, 2002), (6) onset of North American glaciation (Haug et al., 2005), (7) onset of glaciation within the Olympics (Easterbrook, 1986), (8) change in the deformational style of accretionary wedge offshore the Olympics (Flueh et al., 1998). Convergence rate and angle are from Doubrovine and Tarduno (2008).

**Table 1:** Data for the ocean drill cores shown in Fig. 3.

| Core | ODP 888 | OPD 1027 | DSDP 174 |
|---|---|---|---|
| Drilled/total sediment thickness[a] (m) | 570/2600 | 620/620 | 880/910 |
| Cored Quaternary sediment (m) | 570 | 460 | 430[b] |
| Maximum age of Quaternary sediments[c] (Ma) | 0.6 | 1.7 | 1.7 |
| Amount of Quaternary section of total core (%) | - | 74 | 47 |
| Age of oceanic crust[d] (Ma) | 6.5 | 3.2 | 7.5 |
| Quaternary sedimentation rate (m/Myr) | 950[e] | 270 | 250 |
| Pre-Quaternary/total sedimentation rate[f] (m/Myr) | -/400 | 110/190 | 80/120 |

920 **Notes:** For core ODP 888 information is taken from Westbrook et al. (1994), for ODP 1027 from Su et al. (2000), and for DSDP 174 from Kulm et al. (1973). Sedimentation rates are calculated in this study using the reported thicknesses and age constraints.
[a]: If total thickness exceeds drilled thickness, then the total thickness was estimated from seismic data (e.g., ODP 888).
[b]: Due to poor core recovery, the Plio-Pleistocene boundary can only be confined to be between 418 and 446 m.
[c]: Ages based on biostratigraphy, for cores ODP 1027/DSDP 174 the Plio-Pleistocene boundary was recovered and an age of 1.7 Ma is used
925 here as reported by Su et al. (2000).
[d]: For cores ODP 888/DSDP 174, the age refers to the age of the oceanic crust and is taken from Fig. 3 at the respective location of the core. For ODP 1027, the age refers to the age of the oldest sediment in the core taken from Su et al. (2000).
[e]: This rate is calculated for the recovered core interval, which only encompasses 600 ka.
[f]: Total sedimentation rate = total thickness divided by age of oceanic crust.

930

935

940

945    **Table 2:** Coordinates, elevation and thermochronometric cooling ages for samples considered in this study.

| Sample | Latitude (°) | Longitude (°) | Elevation (m) | AHe ± 1SD (Ma) | AFT ± 1SD (Ma) | ZHe ± 1 SD (Ma) | ZFT ± 1SD (Ma) |
|---|---|---|---|---|---|---|---|
| **Mount Olympus transect samples** | | | | | | | |
| *OP1533[a]* | *47.87572* | *-123.69427* | *430* | *2.5 ± 0.4* | *5.1 ± 0.6* | *4.8 ± 0.6* | *unreset* |
| OP1550 | 47.81568 | -123.69601 | 1825 | 2.0 ± 0.7 | nd | 7.0 ± 0.8 | nd |
| *OP1551* | *47.82647* | *-123.68324* | *1509* | *3.3 ± 0.6* | *6.2 ± 0.8* | *7.0 ± 0.5* | *unreset* |
| OP1552 | 47.80155 | -123.71102 | 2377 | 3.7 ± 0.2 | nd | 8.5 ± 1.5 | unreset |
| OP1553 | 47.80377 | -123.70244 | 2188 | 2.9 ± 1.6 | nd | 7.6 ± 0.4 | nd |
| OP1554 | 47.83979 | -123.69330 | 1222 | 1.9 ± 0.8 | nd | 7.1 ± 0.5 | nd |
| OP1555 | 47.85457 | -123.69194 | 851 | 2.5 ± 1.0 | nd | 7.2 ± 1.3 | nd |
| **Blue Mountain transect samples** | | | | | | | |
| OP1548[a] | 48.02186 | -123.34295 | 410 | 14.8 ± 1.2 | nd | unreset | nd |
| OP1557 | 47.98098 | -123.31173 | 917 | 4.4 ± 2.5 | nd | nd | nd |
| OP1558 | 47.97233 | -123.30092 | 1032 | 8.6 ± 1.2 | nd | unreset | nd |
| OP1559 | 47.97287 | -123.28636 | 1184 | 10.8 ± 1.9 | nd | nd | nd |
| OP1560 | 47.96709 | -123.27110 | 1324 | unreset | nd | nd | nd |
| OP1561 | 47.95783 | -123.26785 | 1500 | 30.1 ± 2.0 | nd | nd | nd |
| OP1562 | 47.95696 | -123.26078 | 1778 | 3.6 ± 1.3 | nd | unreset | nd |
| **Mount Anderson transect samples** | | | | | | | |
| OP1570 | 47.70483 | -123.32813 | 1624 | nd | nd | 8.2 ± 1.1 | nd |
| OP1571 | 47.71657 | -123.32927 | 2035 | 3.0 ± 0.5 | nd | 8.1 ± 0.9 | nd |
| OP1572[b] | 47.71473 | -123.32815 | 1842 | 3.3 ± 0.4 | nd | 8.4 ± 1.4 | nd |
| *OP1573* | *47.69400* | *-123.32765* | *1363* | *3.9 ± 0.4* | *7.8 ± 1.5* | *8.9 ± 0.9* | *nd* |
| OP1574 | 47.68899 | -123.35093 | 881 | 3.1 ± 1.1 | nd | 7.8 ± 0.9 | nd |
| OP1576[b] | 47.67451 | -123.39235 | 614 | 1.5 ± 0.2 | nd | 6.5 ± 0.2 | nd |
| OP1577 | 47.64185 | -123.43398 | 470 | nd | nd | 7.0 ± 0.8 | nd |
| **Equal elevation samples** | | | | | | | |
| OP1502[a] | 47.90796 | -122.92804 | 325 | unreset | unreset | unreset | nd |
| OP1510[a] | 48.09852 | -123.62231 | 273 | 8.3 ± 1.2 | unreset | unreset | nd |
| *OP1513[a]* | *47.96015* | *-123.57273* | *402* | *1.5 ± 0.3* | *5.7 ± 0.7* | *10.2 ± 1.0* | *unreset* |
| *OP1517[a]* | *47.93891* | *-123.51376* | *423* | *3.7 ± 0.9* | *5.0 ± 0.8* | *9.0 ± 0.6* | *unreset* |
| OP1521[a] | 48.04832 | -124.08702 | 390 | 2.0 ± 0.4 | unreset | unreset | nd |
| OP1522[a] | 48.00530 | -124.41620 | 367 | 9.1 ± 0.9 | unreset | unreset | nd |
| OP1527[a] | 47.82500 | -124.05184 | 280 | 2.8 ± 1.0 | unreset | unreset | nd |
| OP1528 | 47.80681 | -123.99661 | 140 | 3.0 ± 0.3 | unreset | nd | nd |
| OP1529[a] | 47.78265 | -124.14257 | 343 | 6.2 ± 1.1 | unreset | unreset | nd |
| OP1531[a] | 47.63659 | -124.34966 | 50 | 7.5 ± 0.5 | unreset | unreset | nd |
| *OP1539[a]* | *47.64151* | *-123.65870* | *446* | *2.1 ± 0.6* | *7.1 ± 0.9* | *6.8 ± 0.4* | *12.6 ± 1.5* |
| OP1542[a] | 47.56001 | -123.37533 | 450 | 1.9 ± 0.7 | unreset | 8.6 ± 0.9 | nd |
| OP1556 | 48.00848 | -123.89398 | 470 | 3.3 ± 0.9 | nd | nd | nd |
| *OP1582[a]* | *47.95595* | *-123.83732* | *578* | *1.7 ± 0.5* | *6.0 ± 0.6* | *7.1 ± 0.5* | *unreset* |

**Notes:** Samples in italics are used for 1D thermo-kinematic modelling. Results from single grain analyses for AHe and ZHe are reported in Tables DR1 and DR2, respectively. Further details for AFT and ZFT dating can be found in Table 3, and single grain analyses for apatite and zircon are reported in Tables DR3 and DR4, respectively. 1SD = one standard deviation, nd = not determined.

950    [a]: AHe and ZHe ages of the respective samples are from Michel et al. (2018).
[b]: Reported sample AHe ages are single-grain ages, because the yield of suitable apatite grains did not allow to date more grains.

**Table 3:** Results from fission-track dating.

**Reset samples**

| Sample +Mineral | Grain ages (Ma) | $\chi^2$ (%) | N | reset state | Sample age ± 1SD (Ma) |
|---|---|---|---|---|---|
| OP1513 ap | 0.9–17 | 47 | 24 | R | 5.7 ± 0.7 |
| OP1517 ap | 0–13 | 25 | 17 | R | 5.0 ± 0.8 |
| OP1533 ap | 2–15 | 11 | 20 | R | 5.1 ± 0.6 |
| OP1539 ap | 3–31 | 21 | 21 | R | 7.1 ± 0.9 |
| OP1539 zr | 8–18 | 19 | 21 | R | 12.6 ± 1.5 |
| OP1551 ap | 0–16 | 76 | 21 | R | 6.2 ± 0.8 |
| OP1573 ap | 5–17 | 11 | 6 | R | 7.8 ± 1.5 |
| OP1582 ap | 0–19 | 55 | 22 | R | 6.0 ± 0.6 |

**Notes:** For AFT and ZFT 20 grains are dated in a first step and it is checked whether the sample passes the $\chi^2$-test and can be considered as reset (i.e., > 5%; an indication for belonging to the same age population, e.g., Galbraith, 2005). If so, the pooled ζ-age is considered as the sample age and reported in the table. If a sample fails the $\chi^2$-test (i.e., < 5%), the sample is considered unreset and, in the case of AFT, 100 grains are dated if enough grains are available. The detrital age distribution is then decomposed into detrital age populations using BINOMFIT (Brandon, 1992, 1996) and the peak ages of those populations (with asymmetric error range for each age peak, corresponding to the 68% confidence interval, CI) are reported in the table. For the ZFT method, the information whether the sample is reset or unreset is sufficient for this study and no further grains are dated. Fraction equals the amount of grains contained within the respective age peak. N=number of counted grains. Contrary to Brandon et al. (1998) we do not consider multiply or partially reset AFT samples but treat them as unreset, because our thermo-kinematic model can only be applied to fully reset samples.
[a]: Results for this sample are obtained by merging grains from our sample OP1527 (n=103) and sample AR39 (n=31) from Brandon et al. 1998).
[b]: Results for this sample are obtained by merging grains from our sample OP1528 (n=68) and sample AR40 (n=12) from Brandon et al. (1998).

**Unreset samples** / Age peaks of the age populations

| Sample +Mineral | Grain ages (Ma) | $\chi^2$ (%) | N | reset state | Age (Ma) | 68% CI (Ma) | | Fraction (%) | Age (Ma) | 68% CI (Ma) | | Fraction (%) | Age (Ma) | 68% CI (Ma) | | Fraction (%) |
|---|---|---|---|---|---|---|---|---|---|---|---|---|---|---|---|---|
| OP1502 ap | 10–630 | 0 | 94 | UR | 25.9 | -2.5 | +2.7 | 29.4 | 84.7 | -8.1 | +9.0 | 48.3 | 243 | -54.6 | +70.0 | 22.2 |
| OP1510 ap | 18–191 | 0 | 80 | UR | 35.5 | -5.4 | +6.4 | 34.5 | 52.6 | -6.0 | +6.8 | 52.9 | 100.3 | -23.6 | +30.7 | 12.6 |
| OP1513 zr | 17–82 | 0 | 23 | UR | 30.9 | -3.5 | +4.0 | 70.9 | 52.6 | -7.5 | +8.8 | 29.1 | - | - | - | - |
| OP1517 zr | 27–57 | 0 | 25 | UR | 33.7 | -8.0 | +10.5 | 15.5 | 41.4 | -4.5 | +5.1 | 84.5 | - | - | - | - |
| OP1521 ap | 0.5–499 | 0 | 103 | UR | 9.8 | -0.8 | +0.8 | 60.5 | 35.1 | -4.0 | +4.5 | 30.6 | 261.9 | -50.4 | +62.2 | 8.9 |
| OP1522 ap | 6–237 | 0 | 20 | UR | 16.3 | -2.8 | +3.4 | 20.2 | 41.8 | -3.5 | +3.8 | 59.7 | 130.1 | -32.7 | +43.5 | 20 |
| OP1527[a] ap | 1–992 | 0 | 134 | UR | 7.4 | -0.5 | +0.6 | 67.7 | 24.0 | -2.0 | +2.2 | 28.0 | 209.3 | -65.4 | +94.5 | 3.5 |
| OP1528[b] ap | 0.4–237 | 0 | 80 | UR | 4.7 | -0.4 | +0.4 | 75.7 | 14.6 | -2.2 | +2.5 | 24.1 | - | - | - | - |
| OP1531 ap | 6–684 | 0 | 100 | UR | 10.7 | -0.5 | +0.6 | 50.6 | 30.2 | -1.8 | +1.9 | 40.1 | 149.0 | -21.7 | +25.3 | 6.5 |
| OP1533 zr | 29–106 | 0 | 23 | UR | 35.6 | -4.0 | +4.5 | 43.5 | 53.5 | -5.7 | +6.4 | 47.7 | 95.8 | -12.5 | +14.3 | 8.7 |
| OP1542 ap | 3–43 | 0 | 19 | UR | 8.1 | -0.8 | +0.9 | 77.1 | 27.9 | -3.6 | +4.2 | 22.9 | - | - | - | - |
| OP1551 zr | 9–57 | 0 | 23 | UR | 15.1 | -1.8 | +2.0 | 62.7 | 25.5 | -3.6 | +4.1 | 21.0 | 49.9 | -6.5 | +7.4 | 16.3 |
| OP1552 zr | 10–38 | 0 | 24 | UR | 14.0 | -1.5 | +1.7 | 79.7 | 32.3 | -3.7 | +4.2 | 20.3 | - | - | - | - |
| OP1582 zr | 28–68 | 0 | 23 | UR | 31.1 | -3.5 | +3.9 | 35.0 | 52.1 | -5.5 | +6.2 | 65.0 | - | - | - | - |

**Table 4:** List of parameters used for the Pecube modelling.

| Parameter | Value | Source |
|---|---|---|
| Thermal conductivity | 1.83 W m$^{-1}$K$^{-1}$ | average value for six drill cores in sediment material in the shelf offshore from Vancouver Island (Lewis et al., 1988) |
| Specific heat capacity | 1200 J kg$^{-1}$K$^{-1}$ | |
| Crustal density | 2700 kg m$^{-3}$ | |
| Mantle density | 3200 kg m$^{-3}$ | |
| Temperature at the base of the model | 400 °C | extrapolation to greater depths from temperature estimates based on heat flow measurements on the shelf (Hyndman et al., 1990; Hyndman and Wang, 1993; Booth-Rea et al., 2008) |
| Temperature at sea level | 8 °C | |
| Atmospheric lapse rate | 6.69 °C km$^{-1}$ | |
| Crustal heat production | 0.77 µW m$^{-3}$ | average value from drill cores on the shelf offshore Vancouver Island (Lewis and Bentkowski, 1988) |
| Model depth | 20 km | minimum thickness of the accretionary wedge below the Olympic Mountains (e.g. Davis and Hyndman, 1989) |

**Table 5:** Results from influx and outflux calculations.

| | Accretionary influx over 14 Myr period | | | Denudational outflux over 14 Myr period | | |
|---|---|---|---|---|---|---|
| | Minimum [a] (1.5 km) | Maximum [a] (2.5 km) | Increase at 2 Ma [a] (1.5 → 2.5 km) | Constant rates [b] | 50% increase at 3 Ma [b] | 150% increase at 2 Ma [b] |
| 2D[c] | 520–540 km$^3$ | 980–1020 km$^3$ | 580–600 km$^3$ | 960 km$^3$ | 1060 km$^3$ | 1160 km$^3$ |
| 3D | 68–71 x 10$^3$ km$^3$ | 128–133 x 10$^3$ km$^3$ | 75–78 x 10$^3$ km$^3$ | 72 x 10$^3$ km$^3$ | 80 x 10$^3$ km$^3$ | 88 x 10$^3$ km$^3$ |

**Notes:**

[a]: Sensitivity to incoming sediment thickness: The accretionary influx volume is calculated for three different sediment thicknesses, yielding
10  a minimum volume (1.5 km thickness), maximum volume (2.5 km thickness), and a more realistic volume (where the volume increases from 1.5 km to 2.5 km at 2 Ma).

[b]: Sensitivity to an increase in exhumation rates: The denudational outflux volume is calculated assuming constant exhumation rates, and considering the increase in exhumation rates due to glacial erosion, with an increase by 50% at 3 Ma or an increase by 150% at 2 Ma. Exhumation rates are based on Michel et al. (2018) and displayed in Fig. 6d and e.

15  [c]: Strictly speaking, the volumes calculated for the 2D scenarios have units of km$^2$ or km$^3$ per km of width/depth (of either influx or outflux). However, to not confuse the reader when we talk of volumes, we decided to use the unit km$^3$, which does not change the actual value, but only the unit of the respective calculated volume.